An Infrared Survey Of Supernova Remnants In The Small Magellanic Cloud

Bachelorarbeit aus der Physik

Vorgelegt von

CHRISTOPHER INGENHÜTT

13. November 2018

DR. KARL REMEIS STERNWARTE BAMBERG

FRIEDRICH-ALEXANDER UNIVERSITÄT ERLANGEN-NÜRNBERG

Betreuerin: Prof. Dr. MANAMI SASAKI

Erklärung

Hiermit erkläre ich, dass ich die vorliegende Bachelorarbeit selbstständig verfasst und keine außer den angegebenen Quellen und Hilfsmitteln verwendet habe.

_____   _____

Datum, Ort   Unterschrift

Abstract

Supernova remnants have been studied in great detail at infrared, radio, optical and x-ray wavelengths. A survey of remnants in the Large Magellanic Cloud has revealed an easier infrared detection of these remnants compared to Galactic supernova remnants due to less infrared confusion by the Galactic disc. The supernova remnant population of the Small Magellanic Cloud, which has similar viewing conditions to the Large Magellanic Cloud, has only been surveyed in radio, optical and x-ray analyses so far. In this work, infrared properties of supernova remnants in the Small Magellanic Cloud are studied and comparisons to x-ray data are made. For this, archival data from the Spitzer Space Telescope and AKARI, as well as a source catalogue of ROSAT are used. Morphologies of the remnants in infrared are compared to optical and x-ray morphologies. The infrared fluxes of supernova remnants in the Small Magellanic Cloud at certain wavlengths are then compared to a modified blackbody spectrum to derive dust properties. These properties are compared to Galactic Remnants and remnants in the Large Magellanic Cloud. A detection rate ($\sim 67\%$) that is high compared to Galactic supernova remnants, but similar to those in the Large Magellanic Cloud is found. The dust mass range (0.002 to 0.5 $M_{\odot}$) is found to be similar to both Galactic and Large Magellanic Cloud remnants. The dust temperature range (43 to 57 K) is found to be lower and narrower than that of Galactic and Large Magellanic Cloud remnants. A comparison of the infrared flux at $24\,\mu m$ and the remnants' sizes reveals a correlation. Comparison with the x-ray flux calculated from ROSAT data reveals a correlation between the flux at $24\,\mu m$ and x-ray flux with some outliers. The outliers are the only two oxygen-rich supernova remnants in the Small Magellanic Cloud with relatively lower infrared flux and a third remnant very close to a star-forming region and star cluster with relatively higher infrared flux.

Acknowledgements

Contents

1 Introduction

Supernovae mark the end of the lifespan of stars in a bright explosion that destroys the progenitor star, carries most of its matter away and sends shockwaves into the surrounding medium. Both in the case of thermonuclear supernovae and core-collapse supernovae of massive stars, the explosion shock waves produce so called supernova remnants (SNRs) in the interstellar medium. These SNRs contain interstellar gas, dust from the interstellar medium as well as produced by the supernova ejecta and material expelled by the supernova. Once enough matter is swept up by the shock wave, a secondary shock wave traveling inwards forms. Only the material between these two shock waves is hot. The shock waves accelerate particles to highly relativistic energies, leading to synchrotron radiation of electrons at radio (and sometimes x-ray) wavelengths and cosmic rays. Due to the high temperatures the gas is heated to (10^6 to 10^7 K), thermal radiation from the plasma can be observed at x-ray wavelengths. After the shell cools down far enough (timescale of 10^4 years), recombination of electrons with heavier atoms in the shell sets in, leading to optical line emission. This third evolution phase lasts for $\sim 10^5$ years. After this phase, the SNR grows fainter until it becomes indistinguishable from the surrounding interstellar medium. The dust in SNRs can either be heated by radiative shocks or by collisions with hot plasma. Dust is the origin of infrared (IR) emission in SNRs.

Due to these emission characteristics, studies of SNRs have historically been focused on optical, radio and x-ray data. This has especially been true for surveys of large numbers of SNRs. With data from the all-sky survey of the Infrared Astronomical Satellite (IRAS[1]), a first IR survey of Galactic SNRs in 10 to 100 µm bands became possible. Out of 157 examined objects in Arendt (1989), 51 SNRs with probable IR emission were found. An independent survey of 161 Galactic SNRs (Saken, Fesen, and Shull, 1992) found 44 SNRs with clear or possible IR detections. These two surveys revealed IR emission related to the SNRs in about 30% of the known SNRs. Some morphological similarities of IR emission to radio and x-ray emission were found. Arendt (1989) also showed morphological similarities between IR and optical emission, which points to significant contributions of line emission to the IR spectra. These contributions could not be confirmed at the time. Saken, Fesen, and Shull (1992) also discussed the spectra and found them dominated by thermal emission from dust, with ratios between different wavelengths being an indicator for SNR age. Young SNRs were found to emit more strongly in 12 and 25 µm bands while older SNRs do so at 60 and 100 µm.

The next instrument enabling more SNR studies in the IR spectrum was the Infrared Space Observatory (ISO[2]). Due to its limited field of view (pointing away from sun, earth, moon and Jupiter at varying minimum degrees) however, only a few selected SNRs were observed with it. Douvion et al. (2001) and Douvion, Lagage, and Pantin (2001) identified detailed IR structures and derived conclusions on the physical origin of IR emission in Cas A, Kepler and Tycho SNRs as well as the Crab nebula.

Several years later the AKARI[3] satellite provided an All-Sky survey at wavelengths between 1.7 and 180 µm leading to the first IR detection of a SNR in the Small Magellanic Cloud (SMC) (Koo et al., 2007). The SNRs in the Magellanic Clouds had already been studied in depth in optical, radio and x-ray bands (for example in Mathewson et al., 1984;

---

[1] *Infrared Astronomical Satellite*. URL: https://irsa.ipac.caltech.edu/Missions/iras.html (Accessed: 10 Nov. 2018).

[2] *Infrared Space Observatory*. URL: https://www.cosmos.esa.int/web/iso (Accessed: 10 Nov. 2018).

[3] *AKARI*. URL: http://www.ir.isas.jaxa.jp/AKARI/Observation/ (Accessed: 10 Nov. 2018).

Heyden, Bleeker, and Kasstra, 2004; Filipović et al., 2005).

With AKARI data and finally the data from the Surveying the Agents of a Galaxy's Evolution (SAGE) survey done by the Spitzer Space Telescope[4] and its sister survey SAGE-SMC, SNRs in both the Large Magellanic Cloud (LMC) and the SMC could now be studied in detail in IR. Both of these galaxies have a distinct advantage over studying Galactic SNRs in that their viewing angles are further from the Galactic plane, leading to less confusion by background and foreground sources.

The Spitzer Space Telescope's two IR cameras cover a wide range of wavelengths, with the Infrared Array Camera (IRAC) operating at 3.6, 4.5, 5.8 and 8.0 μm and the Multiband Imaging Photometer (MIPS) at 24, 70 and 160 μm. A survey of SNRs in the LMC has been made based on Spitzer and AKARI data, finding a significantly higher IR detection rate for SNRs when compared to Galactic SNRs, a correlation between supernova type and brightness, constraints on dust mass and dust temperature, dominating dust species, and several other properties from comparison with multiwavelength data (Seok, Koo, and Onaka, 2013).

In this bachelor thesis, SNRs in the SMC are studied in all IRAC and MIPS bands, examining similarities and differences to LMC and Galactic SNRs. Constraints on dust mass and temperature are calculated and potential correlations between IR flux and SNR size as well as IR flux and x-ray flux are explored.

---

[4]*Spitzer Space Telescope.* URL: http://www.spitzer.caltech.edu/ (Accessed: 10 Nov. 2018).

2 Data selection and analysis methods

2.1 Data sets

For the analysis of near-infrared spectra, IRAC data from the SAGE-SMC mission found in the Spitzer Heritage Archive[5] were used. At far-infrared wavelengths, MIPS data from the same mission were used. In both cases, the third and final delivery residual images were used to eliminate point sources. In addition, AKARI data from the Far-infrared All-Sky Survey were used to provide extra data at longer wavelengths.

Despite the AKARI observations having smaller pixel scales than the longest wavelength MIPS images, structures found in MIPS images are sometimes not visible in AKARI images. Due to this apparently lower resolution and the prevalence of stripe artefacts in AKARI images , AKARI data was not used in conjunction with Spitzer data in the analysis.

For a comparison to x-ray data in section 3.2, count rates from the ROSAT PSPC SMC source catalogue[6] were used and fluxes were estimated via the WebPIMMS tool[7] with data from Yokogawa et al. (2000) as model parameters.

2.2 List of supernova remnants

From previous analyses of supernova remnants in the SMC based on optical, radio and x-ray data, a list of remnants (table 1) was established.

Supernova remnant J005800-721101 and candidate J0057.7-7213 are treated as one remnant with elliptical shape due to largely overlapping listed positions and sizes. Haberl et al. (2012) also notes uncertainty whether its x-ray source and the radio source in Filipović et al. (2005) are the same remnant or two. Similarly, due to big overlaps in the described regions, the SNR IKT4 only listed in Badenes, Maoz, and Draine (2010) is seen as the same remnant as J004821-731931 referenced in Filipović et al. (2005) and Haberl et al. (2012). The position listed for IKT4 in Badenes, Maoz, and Draine (2010) is slightly to the north-west of that of J004821-731931, overlapping more than half of its own area with the latter's region. Neither radio (see Filipović et al., 2005), nor optical or x-ray (see figure 4) images suggest the presence of another remnant at that position. This leaves the list at 21 remnants and 3 candidates.

2.3 Extraction regions

Using the positions and sizes listed in Filipović et al. (2005), Haberl et al. (2012) and Badenes, Maoz, and Draine (2010) as a starting point, extraction regions for the remnants were constructed. The source regions were adjusted to include all structures visible in IR images. If the source was too faint to accurately adjust based on IR, x-ray position and size were used.

For background regions, a few different approaches were used. Due to the proximity of

---

[5]*Spitzer Heritage Archive.* URL: https://sha.ipac.caltech.edu/applications/Spitzer/SHA/ (Accessed: 10 Nov. 2018).

[6]*ROSAT PSPC source catalogue.* URL: http://vizier.u-strasbg.fr/viz-bin/VizieR?-source=J/A+AS/142/41 (Accessed: 10 Nov. 2018).

[7]*WebPIMMS tool.* URL: https://heasarc.gsfc.nasa.gov/cgi-bin/Tools/w3pimms/w3pimms.pl (Accessed: 10 Nov. 2018).

index	name	right ascension	declination	size [as]	references	detection	other names	figure
1	J004055-733654	00:40:55.0	-73:36:54.0	174	H, B	radio, x-ray	B0039-7353, DEM S 5	2
2	J004637-730823	00:46:37.6	-73:08:23.3	111	F	IR, radio, x-ray	B0044-73.4	3
3	J004716-730811	00:47:16.6	-73:08:11.5	66	F, H, B	IR, radio, x-ray	B0045-73.4, IKT 2	3
4	J004728-730601	00:47:28.6	-73:06:01.5	165	F, H, B	IR, radio, x-ray	B0045-73.3	3
5	J004741-730930	00:47:41.0	-73:09:30.0	90	H, B	IR, x-ray	J0047.7-7310, (DEM S32)	3
6	J004821-731931	00:48:21.2	-73:19:31.6	111	F, H, B	IR, radio, x-ray	B0046-73.5, DEM S 42E, IKT4	4
8	J004907-731402	00:49:07.8	-73:14:02.0	121	F, H, B	IR, radio, x-ray	B0047-73.5, DEM S 49, IKT 5	5
9	J005110-732121	00:51:08.7	-73:21:21.4	175	F, H, B	radio, x-ray	B0049-73.6, DEM S 53, IKT 6	6
10	J005152-731034	00:51:52.0	-73:10:34.0	97	H, B	x-ray	IKT 7	7
11	J005240-723624	00:52:42.5	-72:37:12.9	302	F, H, B	IR?, radio, x-ray	B0050-72.8, DEM S 68SE	8
13	J005800-721101	00:58:00.0	-72:11:01.4	114	F	IR?, radio, x-ray	B0056-72.4	9
14	J005817-721814	00:58:18.4	-72:17:22.7	210	F, H, B	IR?, radio, x-ray	B0056-72.5, IKT 16	9
15	J005927-721010	00:59:27.7	-72:10:33.6	181	F	IR, radio, x-ray	B0057-72.2, DEM S 103	9
16	J010018-713341	01:00:17.5	-71:32:49.1	137	F, H, B	radio, x-ray	B0058-71.8, DEM S 108	10
17	J010313-720958	01:03:17.4	-72:09:43.0	86	F	IR?, radio	B0101-72.6, IKT 21	11
18	J010329-724728	01:03:29.2	-72:47:23.0	86	H, B	radio, x-ray	J0103.5-7247	12
19	J010402-720149	01:04:01.2	-72:01:52.3	60	F, B	IR, radio, x-ray	B0102-72.3, DEM S 124, IKT 22	11
20	J010505-722319	01:05:08.9	-72:23:16.7	194	F, H, B	IR, radio, x-ray	B0103-72.6, DEM S 125, IKT 23	13
21	J010524-720923	01:05:24.2	-72:09:23.4	149	F, H, B	radio, x-ray	B0104-72.2, DEM S 128	11
22	J010541-720340	01:05:39.0	-72:03:41.0	79	H, B	IR?, radio	DEM S130, J0105.6-7204	11
23	J010619-720527	01:06:20.0	-72:05:28.1	79	F, H, B	IR, radio, x-ray	B0104-72.3, IKT 25	11
candidates								
7	J0049.0-7306	00:49:00.2	-73:06:17.0	45	H	IR, x-ray		3
12	J0056.5-7208	00:56:30.2	-72:08:12.0	103	H	x-ray		9
13	J0057.7-7213	00:57:46.0	-72:13:04.0	144	H	x-ray		9
24	J011333-731704	01:13:33.8	-73:17:04.0	76	F, H, B	IR, radio	N 83C	14

Table 1: List of supernova remnants and candidates analyzed in this work, references are Filipović et al. (2005), Haberl et al. (2012) and Badenes, Maoz, and Draine (2010). Figures refer to figures showing the extraction regions in IR, optical and X-ray wavelengths in section 2.5

some remnants to point sources, star-forming regions or other bright objects not related to the remnants themselves, an annullus could not be applied in all cases. Where possible, an annullus (elliptical for elliptical source regions) was used and constructed based on mainly two characteristics: It must be sufficiently sized to provide good statistics of the background flux, but cannot contain spillover from the remnant itself or other nearby sources.

Where circular or elliptical annulli could not be used due to aforementioned circumstances, a freely-drawn polygon was constructed with the same main characteristics. Section 2.5 shows the extraction regions for sources and background of all analyzed SNRs in 24 μm and source extraction regions in other IR bands, optical and x-ray.

2.4 Data analysis and automated correction

With these defined source and background regions, the fluxes of all remnants were extracted using IDL routines and scripts.

The point source substraction used in IRAC and MIPS data from the SAGE-SMC mission (Gordon et al., 2011) has produced pixels at value 0 (or, in some cases, below that) rather than a value based on the surrounding background. To mitigate this and its effect on the calculated flux, outlier pixels with both very high and very low values were excluded: An automated correction was applied after the first analysis of flux mean and variance to exclude all pixels with values further than 10 sigma from the mean.

Using the scripts *calculatefluxalltypes.pro*, *aperisherr.pro* and *ds9sourcepars.pro*, the total background-substracted flux and error for every SNR was calculated.

2.4.1 IDL scripts

The following section will explain the usage of the three aforementioned IDL scripts. At the end of the section, more in-depth descriptions of the funcionality of all three scripts will be given. Some have extra diagnostics functionalities, which will not be explained or mentioned. Routines in italic occuring in the script subsections are standard IDL routines which are not further explained. The source code for the scripts can be found in Appendix A.

The purpose of these scripts was to automate the process of extracting the fluxes of all SNRs. To achieve this, the main script (*calculatefluxalltypes.pro*) reads out an image file (in .fits format) and two region files (source and background regions in .reg format). It creates a list of SNRs to analyze the fluxes of all SNRs, their errors and size at the wavelength of the image that was read out and creates an output file to write these parameters into.

Going through the list automatically one source at a time, it calls upon the second script (*ds9sourcepars.pro*) to interpret the parameters given by the region files. With these parameters, the main script then extracts pixel values in source and background region to calculate mean and variance. The regions are then modified by excluding pixels that have values further than 10σ from the mean in either direction and the extraction process is repeated.

Finally, the third script (*aperisherr.pro*) calculates an error (in units of pixel values) and the main script converts background-substracted flux, error and size from pixel values and pixel count to [mJy] and [sr].

These values are then written into the output file in the line corresponding to the currently analyzed SNR.

2.4.1.1 *calculatefluxalltypes.pro*

The main script used is *calculatefluxalltypes.pro*. It reads in the .fits file of the wavelength band to analyze and its header for the image size and pixelscale. Then it reads in the source region file and background region file and creates an index of sources. The source and background regions must be two separate files, and corresponding source and background regions must be in the same line in their respective file to be correctly connected. A file to write fluxes and errors into is opened and/or created and a header is written. The next process is repeated for every source on the index created from the source region file:

The second script (*ds9sourcepars.pro*) is called upon to interpret the source region file and provide the parameters necessary to define the source regions within the image file. Only circles and ellipses were assumed as possible source regions, making the following process very similar in both cases. The routines *dist_circle* and *dist_ellipse* are used to determine whether pixels are within the source region, and total pixel value, mean pixel value, pixel count and variance are calculated.

Now the automated outlier correction is applied. A new source region is defined via the routine *where* combining the three conditions that all pixels must be within the old source region, have a pixel value higher than $mean - 10\sigma$ and have a pixel value lower than $mean + 10\sigma$. For this new source region, the same calculation process is repeated to generate total and mean pixel value and pixel count.

The second script (*ds9sourcepars.pro*) is called upon to interpret the background region file and provide the parameters necessary to define the background regions within the im-

age file. In this case, annuli, elliptical annuli and polygons were possible as region types. The annulus and elliptical annulus case are again very similar: Using *where* in combination with *dist_circle* and *dist_ellipse* and combining the conditions of being between the two radii (or half-axis lengths), background regions are analyzed analogously to the source regions. Total pixel value, mean pixel value and variance are again calculated as well as the total background pixel count scaled to the pixel count of the source region.

The polygon case is a bit more complicated. IDL is not very efficient in calculating whether a pixel is within a polygon compared to whether it is within a circle or ellipse, especially for big image sizes. Therefore, a smaller cutout of the image has to be generated. In order to do that, the lowest and highest x– and y–coordinates among all corners of the polygon are used to create a rectangular cutout around the polygon.

In this smaller cutout, the routine *inside* is now fast enough to create an array of the same size as the cutout with value 0 where pixels are not within the polygon and value 1 where pixels are within it. This process reduced calculation time from minutes to fractions of seconds per polygon. The routine *where* can be used to calculate total pixel value, mean pixel value and variance, as well as the total pixel value scaled to the pixel count of the source region.

For background regions, the same correction is applied as for source regions. All region–defining processes are repeated with the conditions of being between $mean - 10\sigma$ and $mean + 10\sigma$ and all values are recalculated.

The third script (*aperisherr.pro*) is called upon to provide the flux error in units of pixel values.

Finally, the pixel values are converted to units of flux using the pixel scale read out from the .fits header and the following values are calculated and saved: total background-substracted flux, error and size of the source region. The source code for this script can be found in appendix A.

2.4.1.2 *ds9sourcepars.pro*

ds9sourcepars.pro is used to analyze the source regions and write their parameters into a matrix with the amount of lines equal to the amount of sources on the index. The current source is then determined to be either a circle or an ellipsis by the amount of parameters it has: circles in ds9 region files have 3 parameters in x–coordinate of the center, y–coordinate of the center and radius.

Ellipses have 5 in x–coordinate of the center, y–coordinate of the center, length of the major–semi axis, length of the minor–semi axis and angle between the major–semi axis and the right ascension axis, in the case of fk5–formatted regions.

If a source region that is not a circle or ellipsis were to be used, the script will output that the source region was misinterpreted and give out the index number.

Similarly to the analysis of the source region, *ds9sourcepars.pro* reads in the parameters of the background region corresponding to the current source. Again, the background region type is determined by the number of parameters: an annullus has 4 parameters in x–coordinate of the center, y–coordinate of the center, radius of the inner circle, radius of the outer circle.

An elliptical annulus has 7, but only 6 are necessary to unambiguously describe the region. The script *ds9sourcepars.pro* reduces the 7 initial parameters to x–coordinate of the center, y–coordinate of the center, axis ratio, angle between the major–semi axis and the right ascension axis, inner major axis and outer major axis. A polygon has an even number greater than 6. Technically, a triangle would have 6 parameters, but for ease of

programming, triangles were ignored as a possibility. The polygon parameters are simply the x– and y–coordinates of all corners. The source code for this script can be found in appendix B.

2.4.1.3   *aperisherr.pro*

aperisherr.pro is used to calculate the flux error from scatter in sky values, random photon noise and uncertainty in mean sky brightness in the background regions. It uses the source region's mean pixel value and pixel count and the background's variance in pixel values and pixel count. The source code for this script can be found in appendix C.

2.5   Supernova remnants

After excluding remnants that were either too faint to be separated from their surroundings or have negative fluxes in several wavelength bands, the list of formerly 21 remnants and 3 candidates is reduced to 14 remnants and 2 candidates detected at IR wavelengths. Images of all remnants at IR, optical and x-ray wavelengths are presented and every remnant is briefly described in the following section. The figures of 9 images each ($3.6, 4.5, 5.8, 8, 24, 70$ and $160\,\mu$m as well as an RGB of S II, H_α and O III and x-ray) are sorted by right ascension in ascending order. The $24\,\mu$m image in the middle of each figure also shows background extraction regions and has a reference bar of 1 arcmin right ascension.

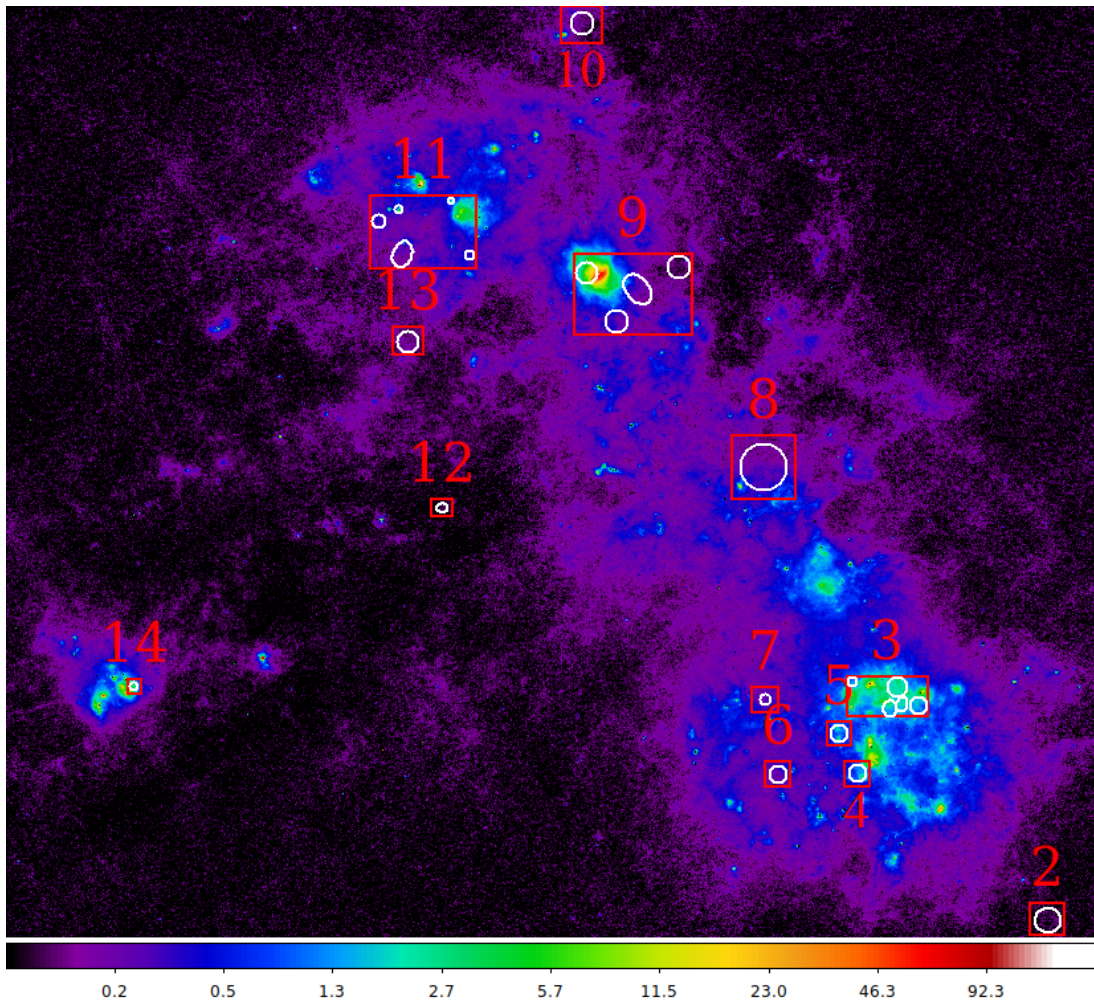Figure 1 is an overview of the following figures at $24\,\mu$m.

Figure 1: Overview of the figures showing extraction regions of the analyzed SNRs and groups of SNRs. Indexes refer to figure numbers.

2.5.1 J004055-733654
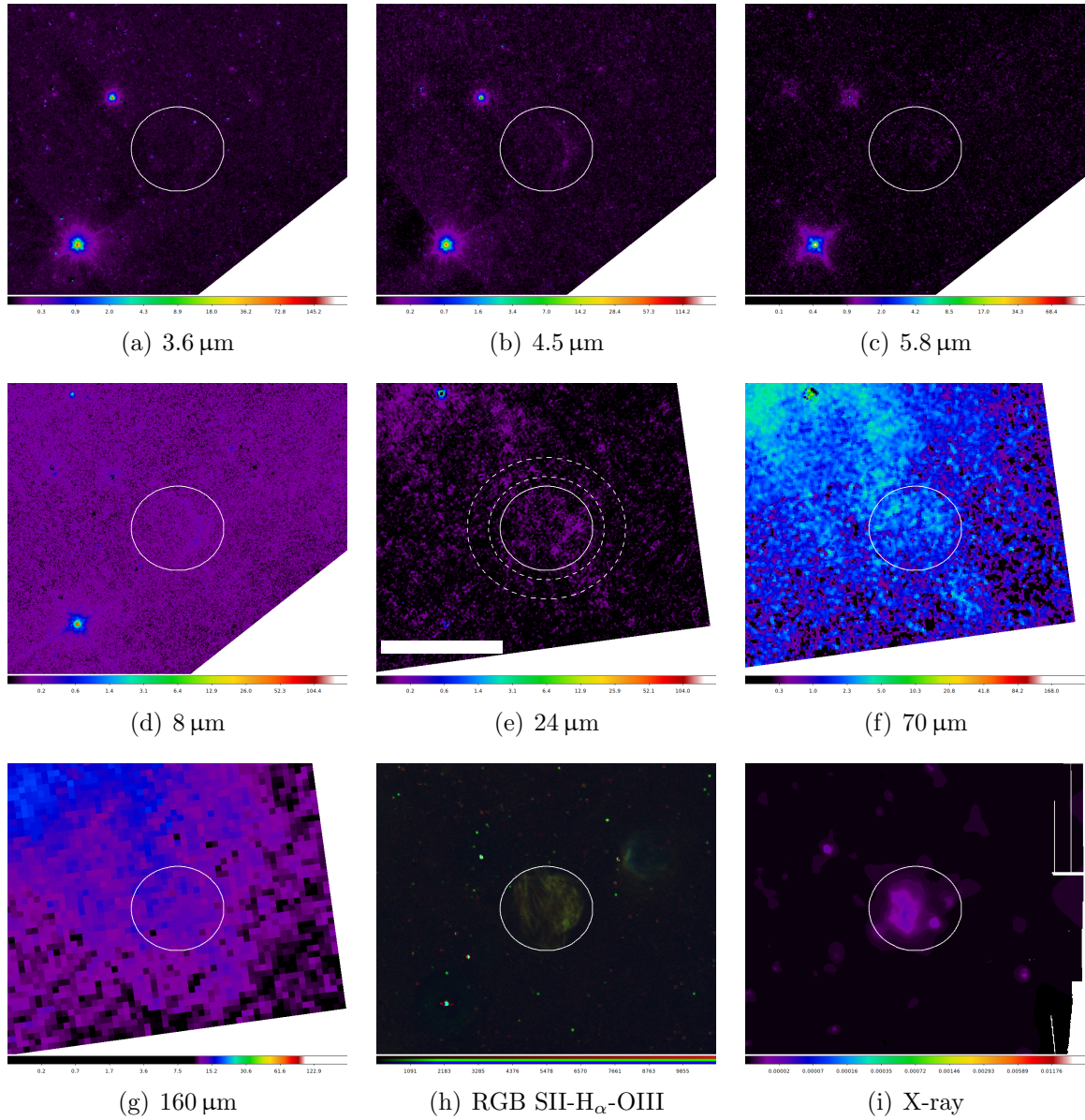
Figure 2: SNR J004055-733654 in 3.6, 4.5, 5.8, 8, 24, 70 and 160 μm IR bands as well as S II, H$_\alpha$ and O III (RGB) and X-ray. White bar above colour scale in 24 μm image represents 1 arcmin right ascension.

Remnant 1 is extremely faint in IR images to the point that the source region was defined exclusively based on x-ray images (see figure 2). The total background-substracted flux is not negative in any of the analyzed bands, but due to the uncertainty whether or not the extracted flux originates from the remnant, its datapoints were marked in red in figures and it was excluded from further analyses. An elliptical annullus is used as the background region.

Southwestern group

There is a group of four SNRs close together in the southwestern part of the SMC bar. For the images, these four remnants have been grouped together with a candidate slightly east of them.
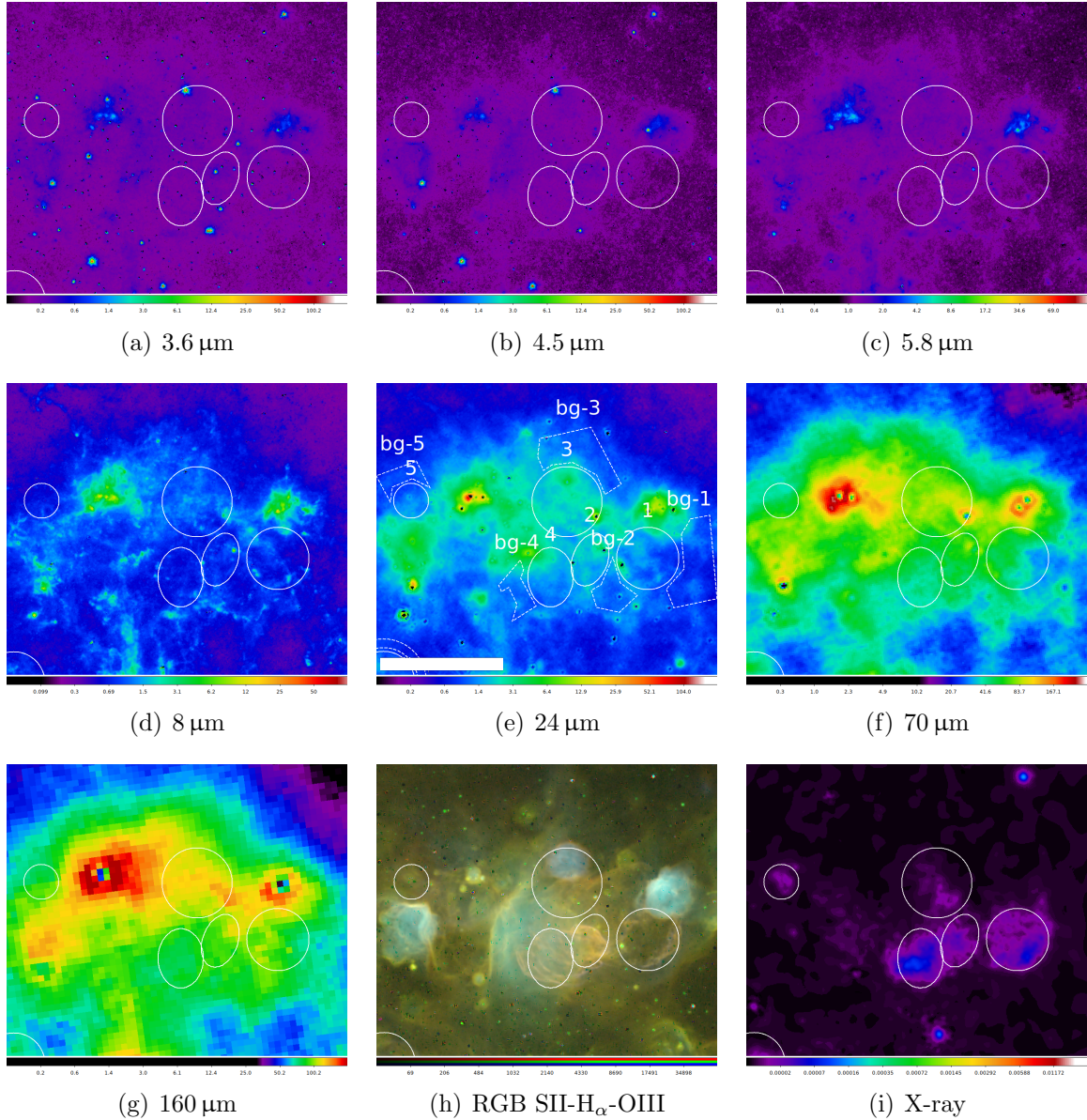
Figure 3: SNRs J004637-730823 (1), J004716-730811 (2) , J004728-730601 (3) and J004741-730930 (4) as well as candidate J004823-730755 (5) in 3.6, 4.5, 5.8, 8, 24, 70 and 160 μm IR bands as well as S II, H$_\alpha$ and O III (RGB) and X-ray. White bar above colour scale in 24 μm image represents 1 arcmin right ascension.

2.5.2   J004637-730823

Remnant 2 with index 1 in figure 3 is visible in most wavelength bands used, only at the shortest two wavelengths (3.6 and 4.5 μm) it is too faint. Due to the proximity to other remnants as well as point sources, a polygon was constructed as the background region.

2.5.3 J004716-730811

The second of four remnants (index 3, index 2 in figure 3) in the southwestern group is visible in all analyzed IR wavelengths and has strongly elliptical shape. A polygon was constructed as the background region to the southwest of the source, because the remnant is neighbour to three other remnants.

2.5.4 J004728-730601

Remnant 4 with index 3 in figure 3 lies north of three very close other remnants, has circular shape and is visible in all analyzed wavelengths. Due to the proximity to the other remnants in the group, a polygon was constructed as the background region north of the remnant.

2.5.5 J004741-730930

The last remnant in this group (index 5, index 4 in figure 3) has elliptical shape and is visible in all analyzed wavelengths. Its background-substracted fluxes are negative in 2 bands, but only in AKARI data. Due to the lower uncertainties and no negative bands in Spitzer data, this remnant's data has not been marked nor excluded from analyses. Due to the proximity of other remnants, a polygon was constructed as the background region.

2.5.6 J0049.0-7306

This supernova remnant candidate with index 7 (index 5 in figure 3) in the figure is very faint at short wavelengths and has a negative background-substracted flux at $3.6\,\mu$m. Due to several point sources close to it, a polygon was constructed as the background region.

2.5.7 J004821-731931

(a) 3.6 μm

(b) 4.5 μm

(c) 5.8 μm

(d) 8 μm

(e) 24 μm

(f) 70 μm

(g) 160 μm

(h) RGB SII-H$_\alpha$-OIII

(i) X-ray
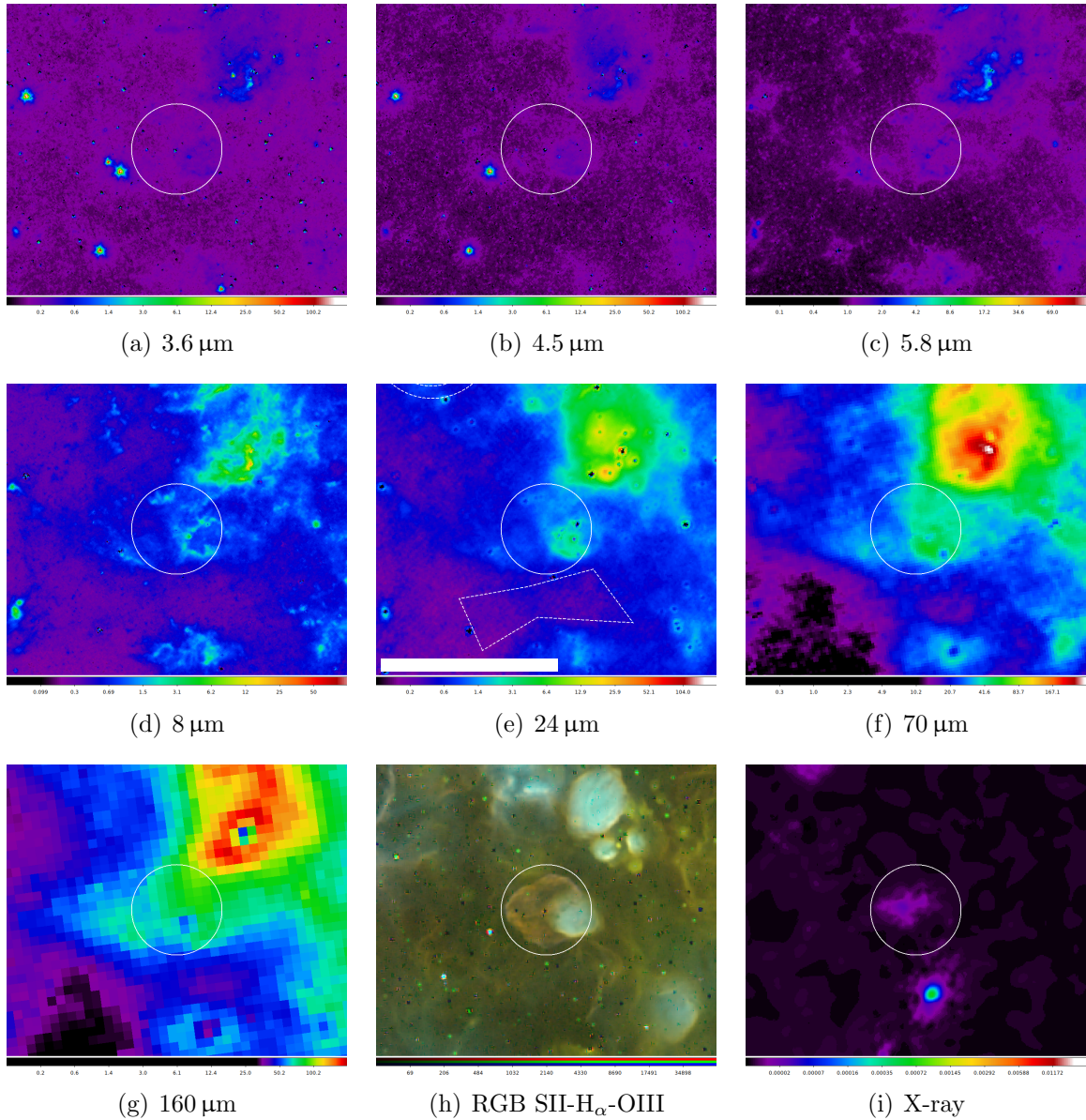
Figure 4: SNR J004821-731931 in 3.6, 4.5, 5.8, 8, 24, 70 and 160 μm IR bands as well as S II, H$_\alpha$ and O III (RGB) and X-ray. White bar above colour scale in 24 μm image represents 1 arcmin right ascension.

Remnant 6 is visible in all analyzed wavelengths and the morphology in 8 and 24 μm images is similar to the one seen in optical images, see figure 4. Due several stars northwest of the remnant in relative proximity, a polygon was constructed as the background region to the south of it.

2.5.8   J004907-731402

(a) 3.6 μm

(b) 4.5 μm

(c) 5.8 μm

(d) 8 μm

(e) 24 μm

(f) 70 μm

(g) 160 μm

(h) RGB SII-H$_\alpha$-OIII

(i) X-ray

Figure 5: SNR J004907-731402 in 3.6, 4.5, 5.8, 8, 24, 70 and 160 μm IR bands as well as S II, H$_\alpha$ and O III (RGB) and X-ray. White bar above colour scale in 24 μm image represents 1 arcmin right ascension.

This supernova remnant with index 8 has a negative background-substracted flux at $3.6 \mu m$, is visible at all other wavelengths and the morphology in 8 and 24 μm images is similar to that in optical images, see figure 5. An annullus was used as the background region.

2.5.9   J005110-732121

(a) 3.6 µm

(b) 4.5 µm

(c) 5.8 µm

(d) 8 µm

(e) 24 µm

(f) 70 µm

(g) 160 µm

(h) RGB SII-H_α-OIII

(i) X-ray

Figure 6: SNR J005110-732121 in 3.6, 4.5, 5.8, 8, 24, 70 and 160 µm IR bands as well as S II, H_α and O III (RGB) and X-ray. White bar above colour scale in 24 µm image represents 1 arcmin right ascension.

The background-substracted flux for remnant 9 is negative in all IRAC bands as well as 160 µm. It is also not visible in IR images, see figure 6. Due to several point sources in the proximity, a polygon was constructed as the background region. Data from this remnant is not used in any further analyses.

2.5.10   J005152-731034

(a) 3.6 µm

(b) 4.5 µm

(c) 5.8 µm

(d) 8 µm

(e) 24 µm

(f) 70 µm

(g) 160 µm

(h) RGB SII-H$_\alpha$-OIII

(i) X-ray
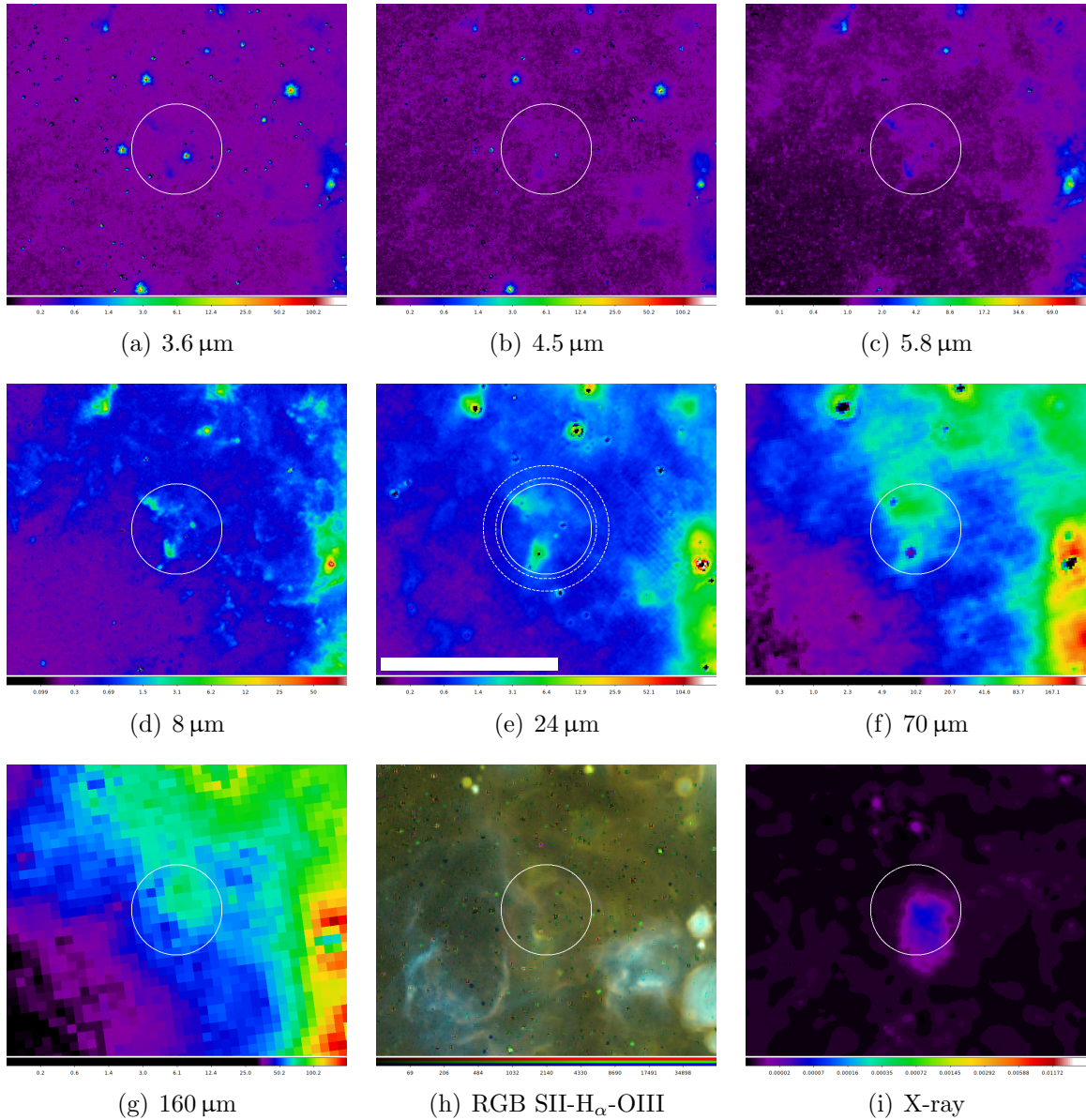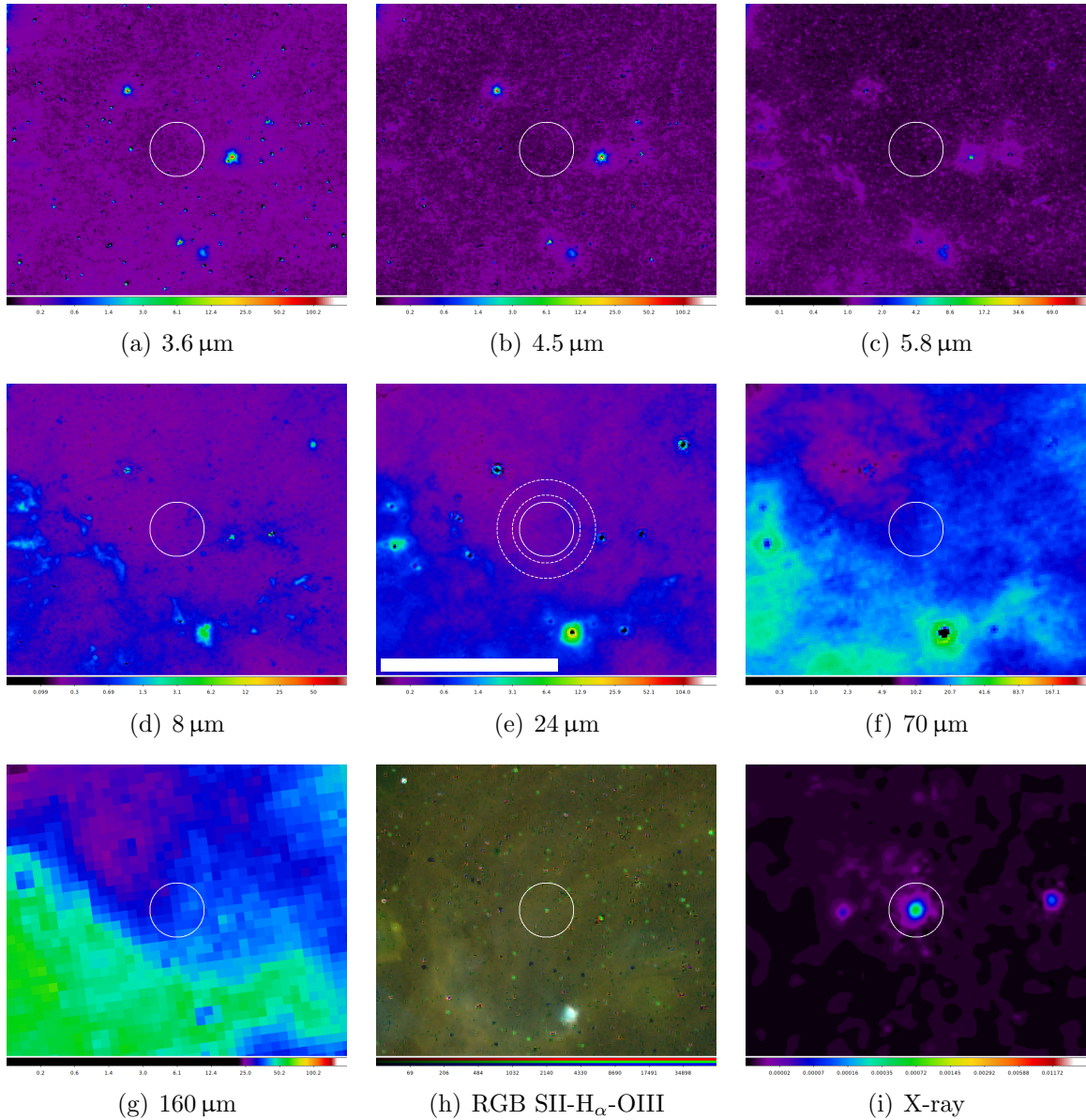
Figure 7: SNR J005152-731034 in 3.6, 4.5, 5.8, 8, 24, 70 and 160 µm IR bands as well as S II, H$_\alpha$ and O III (RGB) and X-ray. White bar above colour scale in 24 µm image represents 1 arcmin right ascension.

All of remnant 10's background-substracted fluxes are negative. An annullus was used as the background region. Data from this remnant was excluded from further analyses. Haberl et al. (2012) noted that this is likely no SNR due to no radio or optical (and IR) counterpart to the extended x-ray source that can be seen in figure 7.
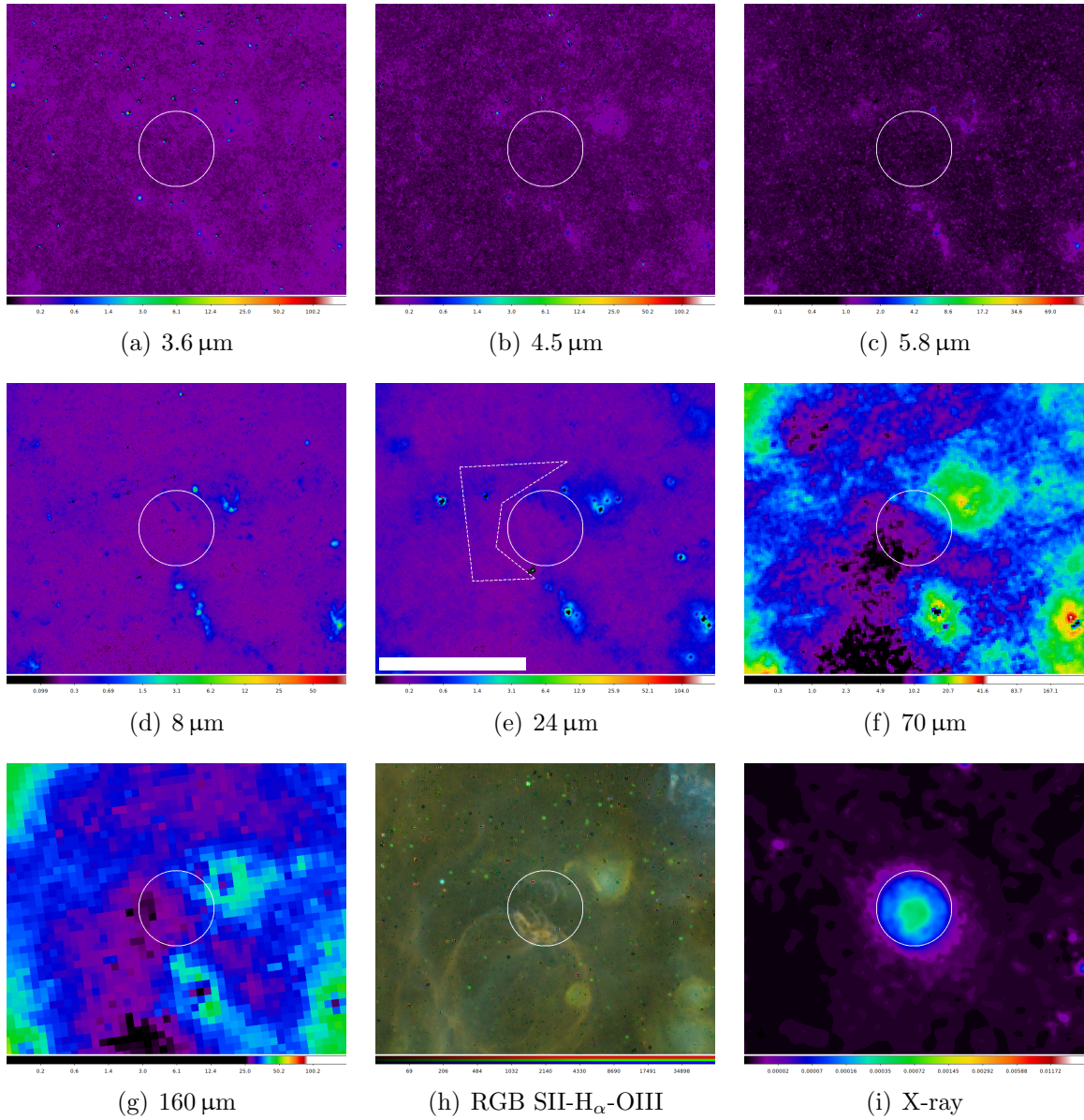
2.5.11 J005240-723624

Figure 8: SNR J005240-723624 in 3.6, 4.5, 5.8, 8, 24, 70 and 160 μm IR bands as well as S II, H$_\alpha$ and O III (RGB) and X-ray. White bar above colour scale in 24 μm image represents 1 arcmin right ascension.

The biggest remnant in the analyzed list, remnant 11, is visible at almost all wavelengths and none of the background-substracted fluxes are negative. At 8 and 24 μm, the morphology is similar to that optical images, see figure 8. The remnant is close to bright point sources, therefore a polygon was constructed as the background region.

Northwestern group

There is another group of remnants in the Northwestern part of the SMC bar. These remnants are not as close together as the southwestern group, however, they were again grouped for images.
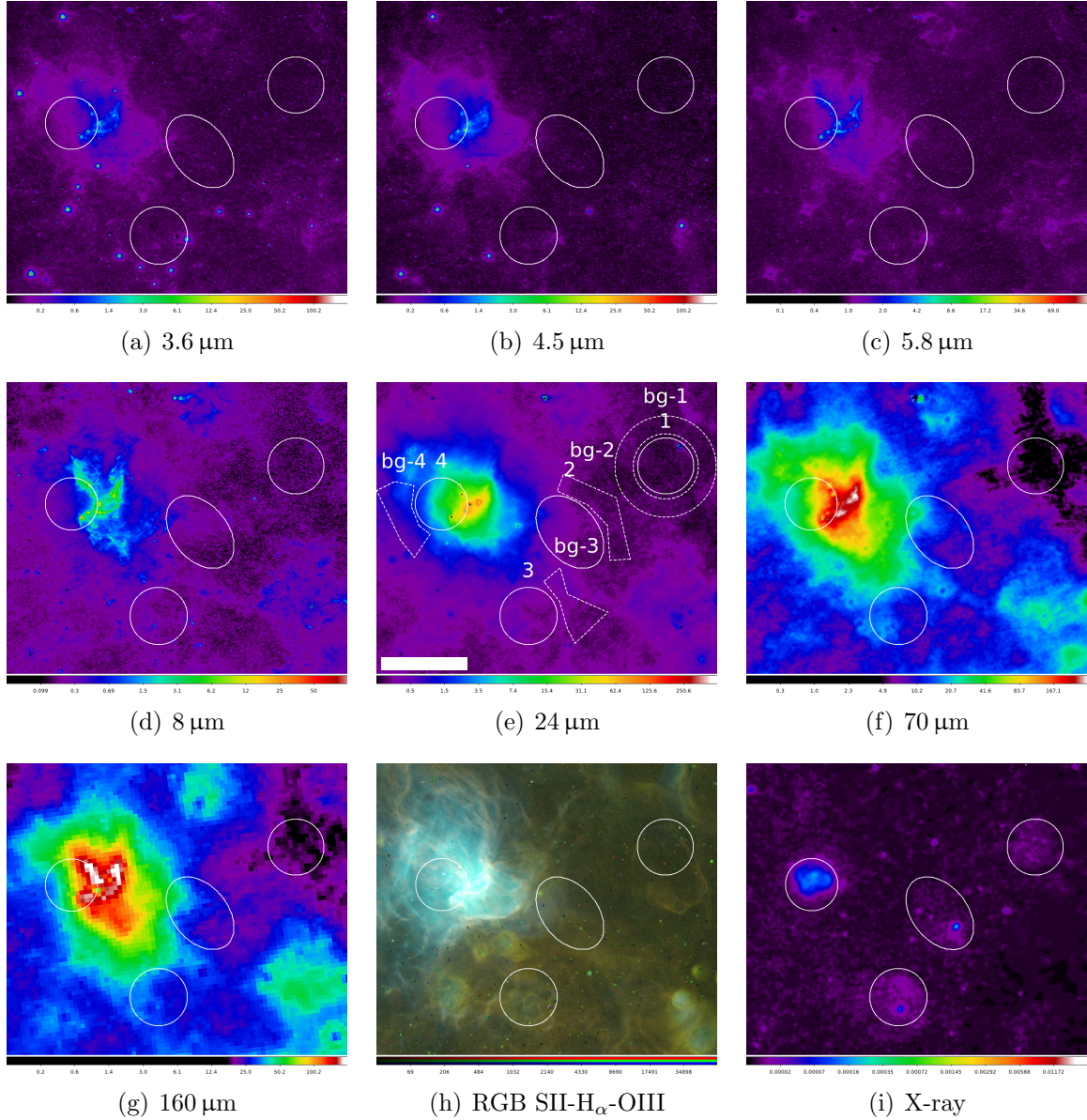
Figure 9: SNR candidate J0056.5-7208 (1) and SNRs J005800-721101 (2), J005817-721814 (3) and J005927-721010 (4) in 3.6, 4.5, 5.8, 8, 24, 70 and 160 μm IR bands as well as S II, H$_\alpha$ and O III (RGB) and X-ray. White bar above colour scale in 24 μm image represents 1 arcmin right ascension.

2.5.12   J0056.5-7208

The supernova remnant candidate with index 12 has index 1 in figure 9, is not visible in IR and has no positive background-substracted fluxes. An annullus was used as the background region. The remnant was excluded from further analyses.

2.5.13 J005800-721101

In the elliptical source region of this remnant (or overlapping remnants, see 2.2, index 13) with index 2 in figure 9, a morphology similar to that in optical images can be seen at 8 and 24 μm. All of the background-substracted fluxes are positive, the remnant is however very faint and hard to separate from the background at lower wavelengths. Due to proximity to the very bright star cluster NGC 346, a polygon was constructed as the background region.

2.5.14 J005817-721814

With index 3 in figure 9, remnant 14 is of circular shape south of the star cluster NGC 346. None of the background-substracted fluxes are negative and it is visible at longer IR wavelengths. Due to the aforementioned star cluster, a polygon was constructed as the background region.

2.5.15 J005927-721010

Remnant 15 (index 4 in figure 9) is directly east of the star cluster NGC 346, point source substraction and the correction outlined in section 2.4 were essential in isolating the flux of the remnant itself. The similarity in morphology between 8 and 24 μm images and optical images helped in constraining the source region to include as little as possible of the star cluster as opposed to the remnant. A polygon was constructed as the background region.

2.5.16   J010018-713341

(a) 3.6 μm

(b) 4.5 μm

(c) 5.8 μm

(d) 8 μm

(e) 24 μm

(f) 70 μm

(g) 160 μm

(h) RGB SII-H$_\alpha$-OIII

(i) X-ray

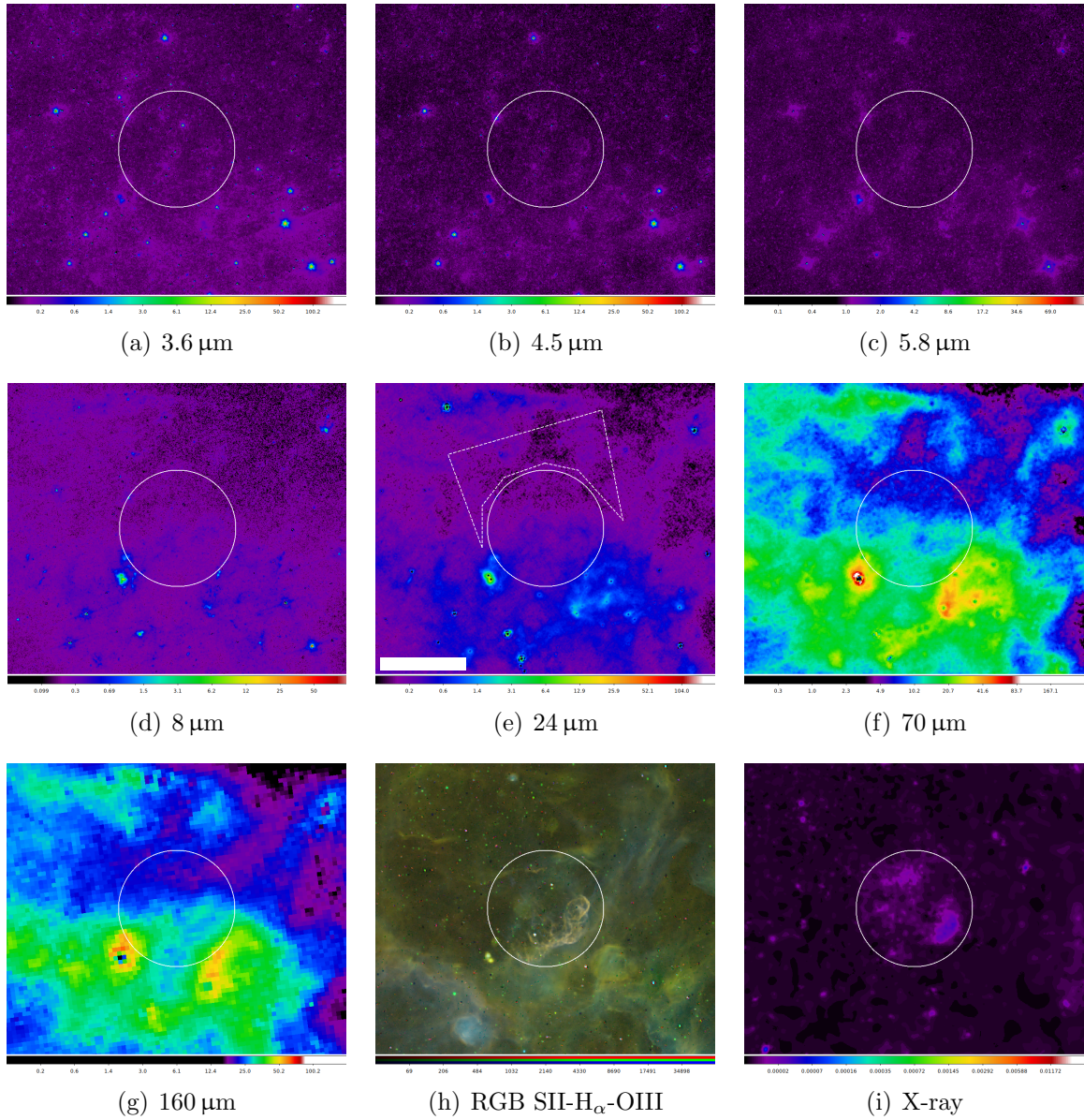Figure 10: SNR J010018-713341 in 3.6, 4.5, 5.8, 8, 24, 70 and 160 μm IR bands as well as S II, H$_\alpha$ and O III (RGB) and X-ray. White bar above colour scale in 24 μm image represents 1 arcmin right ascension.

Remnant 16's background-substracted fluxes are negative or smaller than their calculated error at three of the IRAC wavelengths. Even at longer wavelengths, it is hard to distinguish from the background, see figure 10. The remnant's data points were marked in red in figures and it was excluded from further analyses. Due to two point sources close to the remnant, a polygon was constructed as the background region.

Northern group

In the northern part of the SMC, 5 remnants were again grouped for images.

(a) 3.6 µm

(b) 4.5 µm

(c) 5.8 µm

(d) 8 µm

(e) 24 µm

(f) 70 µm

(g) 160 µm

(h) RGB SII-H$_\alpha$-OIII

(i) X-ray
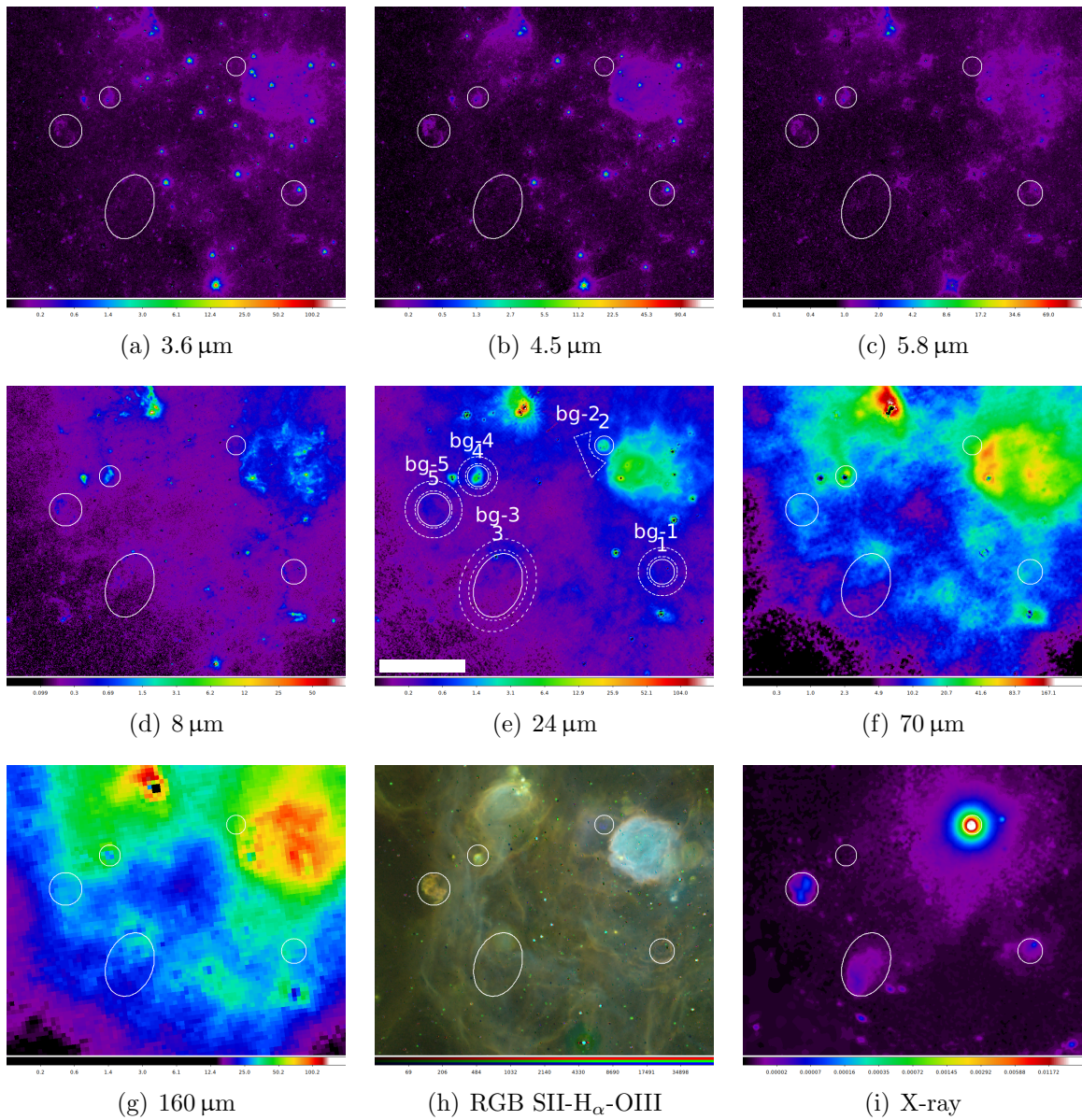
Figure 11: SNRs J010313-720958 (1), J010402-720149 (2), J010524-720923 (3), J010541-720340 (4) and J010619-720527 (5) in 3.6, 4.5, 5.8, 8, 24, 70 and 160 µm IR bands as well as S II, H$_\alpha$ and O III (RGB) and X-ray. White bar above colour scale in 24 µm image represents 1 arcmin right ascension.

2.5.17 J010313-720149

Remnant 17 with index 1 in figure 11 is very faint and has very high variances for the fluxes at higher wavelengths (AKARI data has several datapoints with uncertainties larger than the flux). At lower wavelengths, a bright point source in the source region becomes visible. Due to uncertainty whether this point source is appropriately excluded via the

correction outlined in 2.4 and the aforementioned problems at longer wavelengths, the remnant's data points were marked in red and it was excluded from further analyses. An annullus was used as the background region.

2.5.18 J010402-720149

Remnant 19 has index 2 in figure 11. In addition to exhibiting a morphology very similar to x-ray and optical images at $24\,\mu m$, this remnant is visible at the longer wavelengths and none of its background-substracted fluxes are negative. Due to close proximity to several stars, a polygon was constructed as the background region.

2.5.19 J010524-720923

Remnant 21 has index 3 in figure 11. Its background-substracted fluxes are all negative except for one AKARI band, which is in the same order of magnitude as its uncertainty. The remnant was excluded from further analyses. Due to the elliptical shape, an elliptical annullus was used as the background region.

2.5.20 J010541-720340

Remnant 22 with index 4 in figure 11 is visible at longer wavelengths and exhibits similar morphology at 8 and $24\,\mu m$ compared to optical images. None of its background-susbstracted fluxes are negative. An annullus was used as the background region.

2.5.21 J010619-720527

Remnant 23 with index 5 in figure 11 is visible at all IR wavelengths and exhibits similar morphology to optical images. Some of the background-substracted fluxes are lower than their uncertainties, this is limited to AKARI datapoints and the calculated errors for Spitzer data are far lower. Therefore, the data was not specifically marked in figures using Spitzer data and the remnant was not excluded from further analyses. An annullus was used as the background region.

2.5.22 J010329-724728

(a) 3.6 μm   (b) 4.5 μm   (c) 5.8 μm

(d) 8 μm   (e) 24 μm   (f) 70 μm

(g) 160 μm   (h) RGB SII-H$_\alpha$-OIII   (i) X-ray
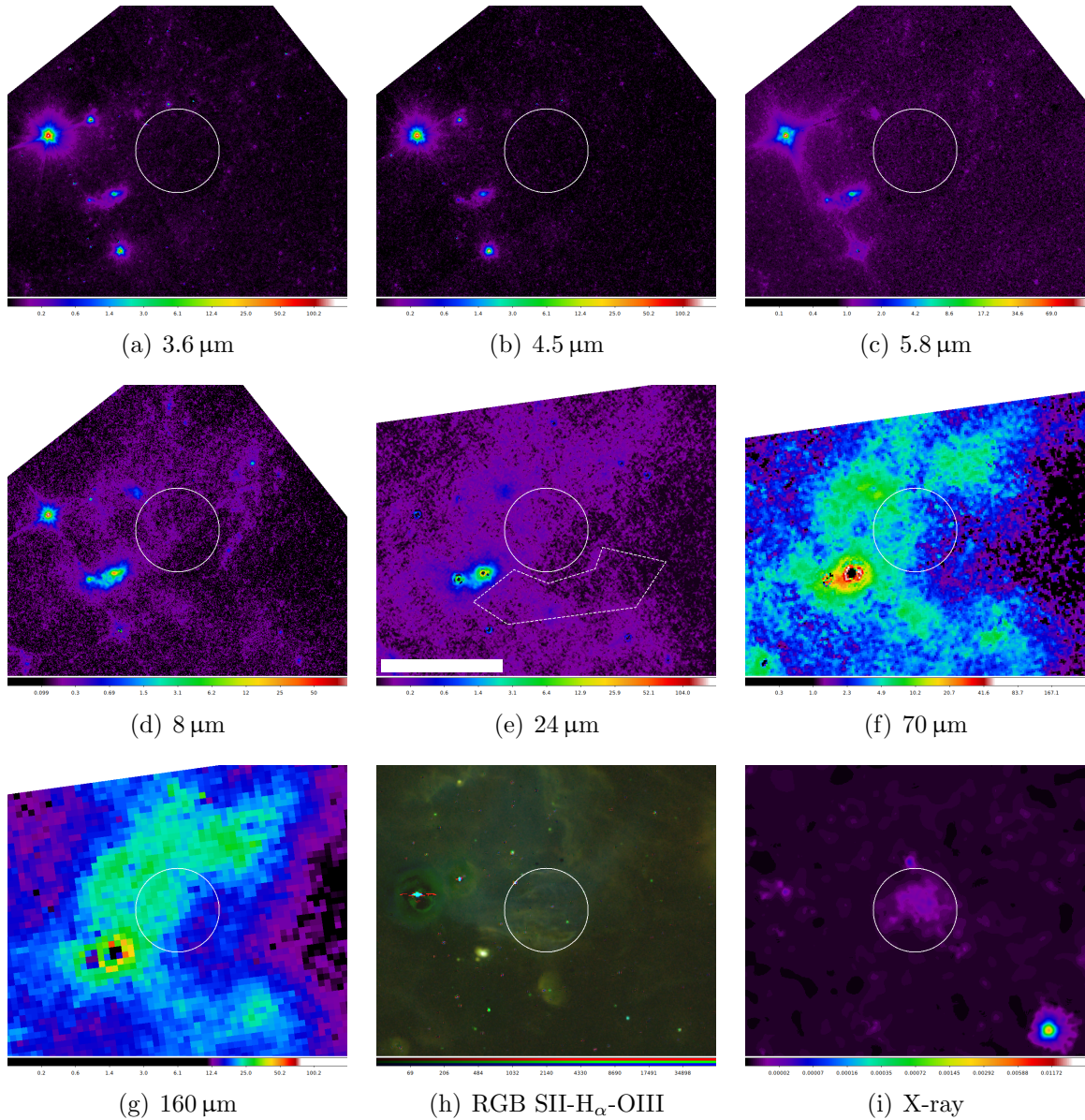
Figure 12: SNR J010329-724728 in 3.6, 4.5, 5.8, 8, 24, 70 and 160 μm IR bands as well as S II, H$_\alpha$ and O III (RGB) and X-ray. White bar above colour scale in 24 μm image represents 1 arcmin right ascension.

Remnant 18's background-substracted fluxes are only positive and larger than their uncertainties at 24, 65 and 70 μm. The source region was defined based on x-ray data and at 24 and 70 μm, the morphology is similar to that in x-ray images, see 12. However, due to the problematic data at other wavelengths, the remnant was excluded from further analyses. An elliptical annullus was used as the background region.

2.5.23   J010505-722319

(a) 3.6 μm

(b) 4.5 μm

(c) 5.8 μm

(d) 8 μm

(e) 24 μm

(f) 70 μm

(g) 160 μm

(h) RGB SII-H$_\alpha$-OIII

(i) X-ray
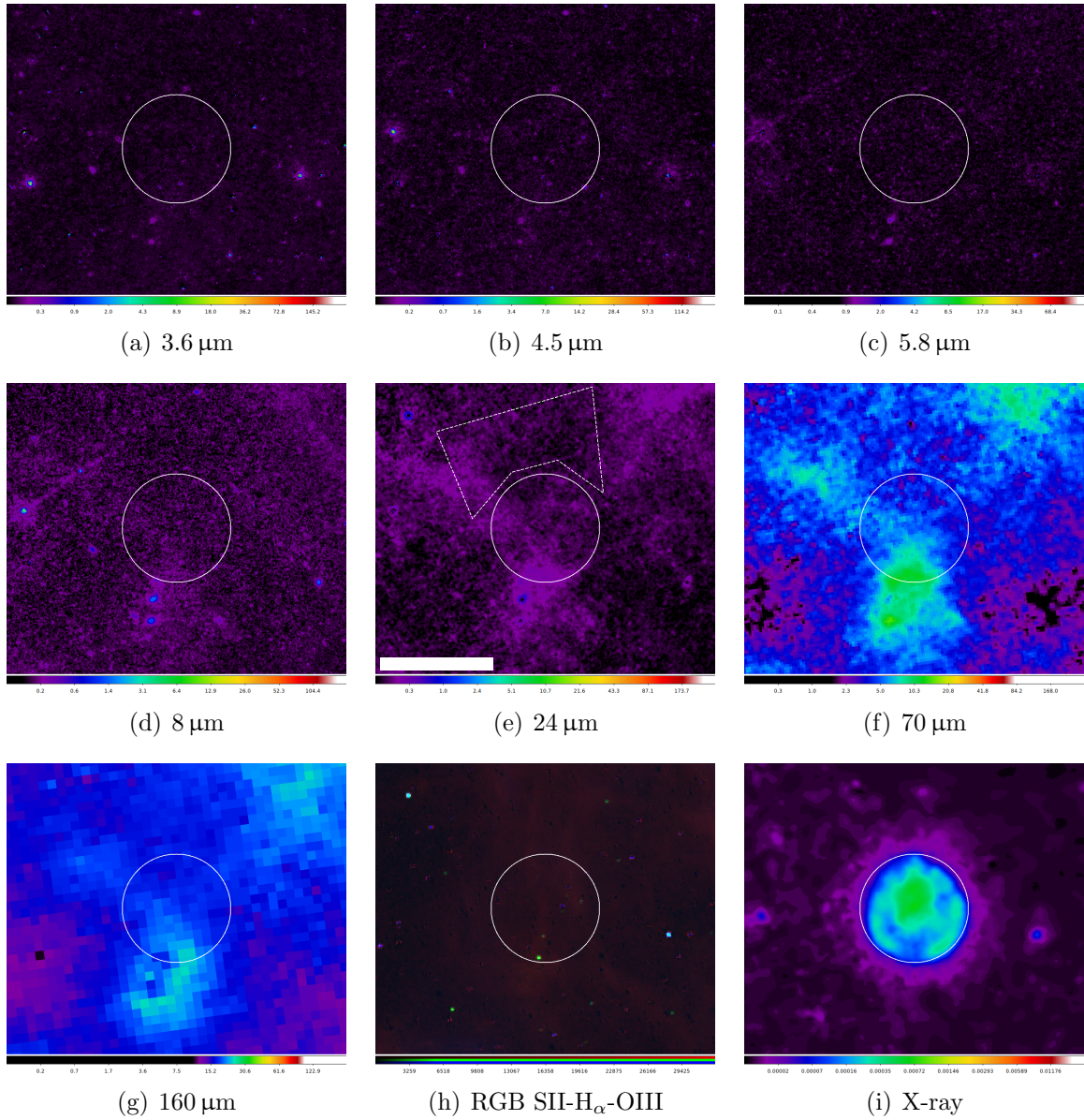
Figure 13: SNR J010505-722319 in 3.6, 4.5, 5.8, 8, 24, 70 and 160 μm IR bands as well as S II, H$_\alpha$ and O III (RGB) and X-ray. White bar above colour scale in 24 μm image represents 1 arcmin right ascension.

None of remnant 20's background-substracted fluxes are negative, two of them are smaller than their uncertainties, however (at 5.8 and 70 μm). It is displayed in 13. Due to a star close to the remnant, a polygon was constructed as the background region.

2.5.24   J011333-731704

(a) 3.6 µm

(b) 4.5 µm

(c) 5.8 µm

(d) 8 µm

(e) 24 µm

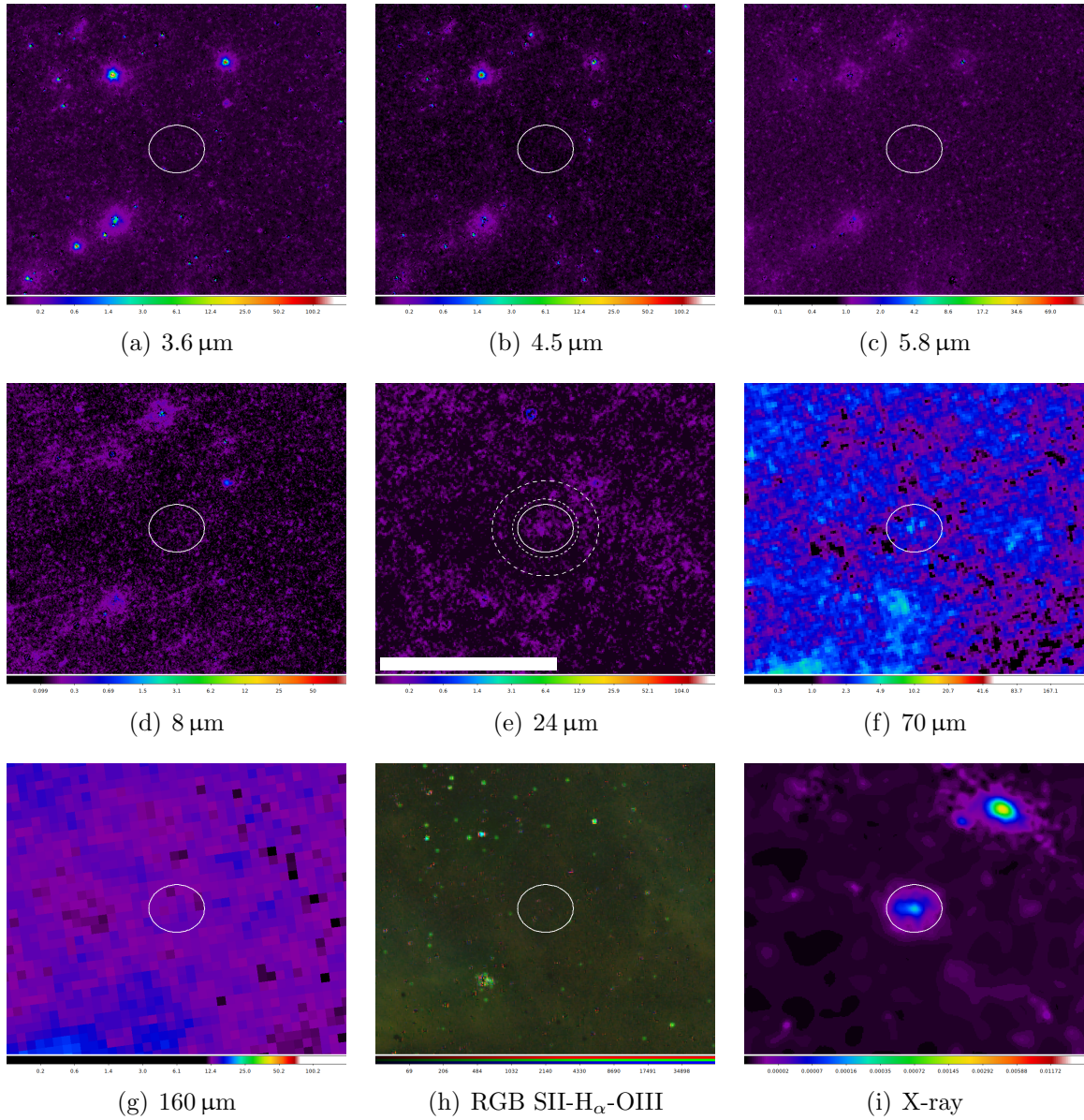(f) 70 µm

(g) 160 µm

(h) RGB SII-H$_\alpha$-OIII

(i) X-ray
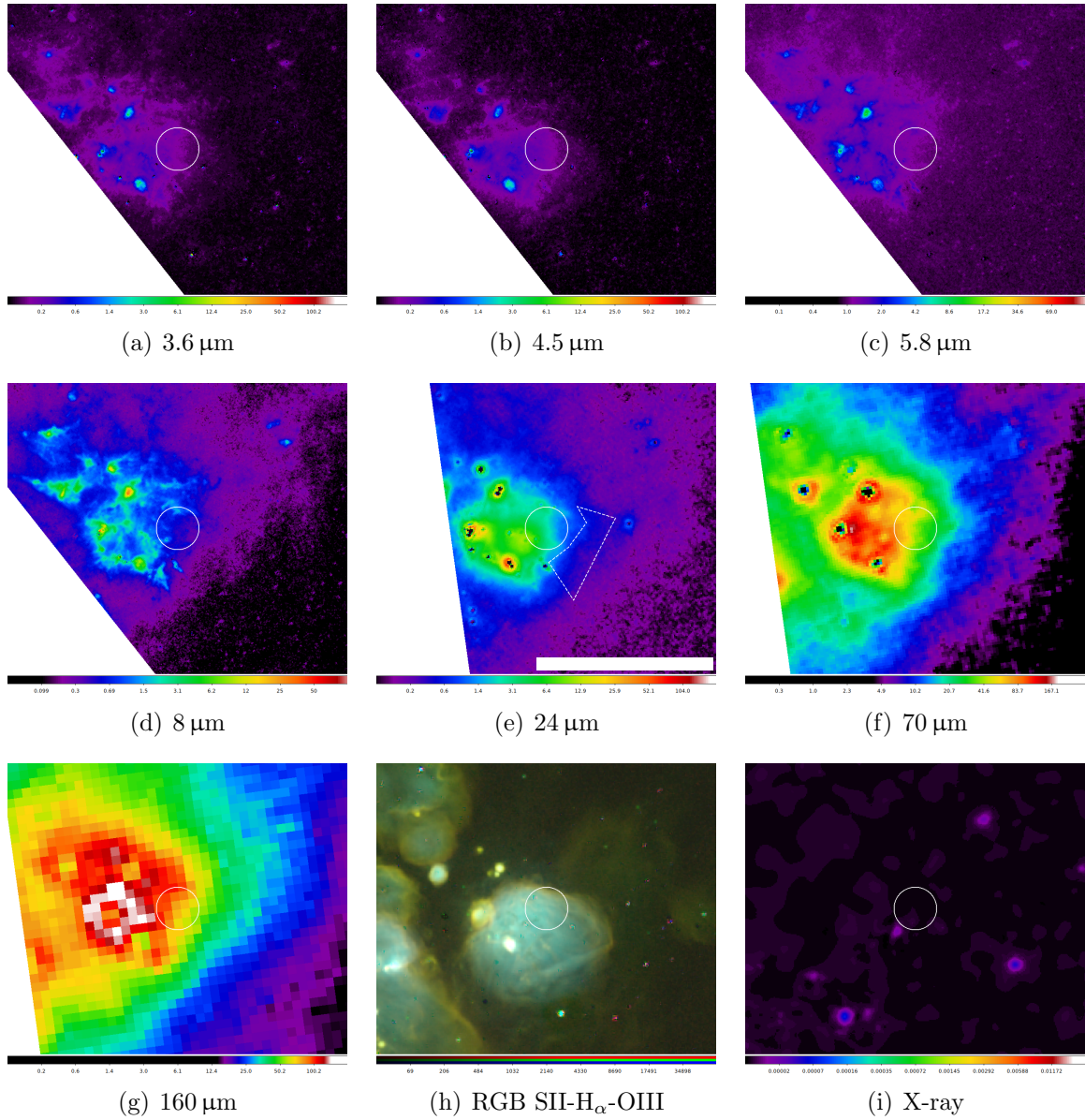
Figure 14: SNR candidate J011333-731704 in 3.6, 4.5, 5.8, 8, 24, 70 and 160 µm IR bands as well as S II, H$_\alpha$ and O III (RGB) and X-ray. White bar above colour scale in 24 µm image represents 1 arcmin right ascension.

This remnant candidate with index 24 is visible at shorter wavelengths moreso than longer ones, see 14. None of the background-substracted fluxes are negative. Due to several bright stars close to the remnant, a polygon was constructed as the background region.

3 Analysis

3.1 Supernova properties from IR fluxes

3.1.1 Dust temperature and dust mass

Table 2 shows the extracted fluxes for all SNRs in Spitzer and AKARI images. SNR names in brackets indicate exclusion from analyses (see section 2.5 for details), background-substracted fluxes lower than their respective uncertainties are listed as upper bounds. Figure 15 shows the SNRs analyzed in this work alongside SNRs analyzed in Seok, Koo, and Onaka (2013) in the 24 μm and 70 μm plane. Assuming that both 24 and 70 μm fluxes originate from dust continuum, the correlation between them can be used to analyze the dust temperature T_{du} and dust mass M_{du} of the SNRs. It should be noted that 24 μm fluxes are not expected to purely originate from dust continuum. To analyze the dust temperature and mass, a modified blackbody spectrum is assumed, following

$$F_\nu = \frac{k_\nu B(\nu, T_{\mathrm{du}}) M_{\mathrm{du}}}{d^2} \tag{1}$$

where F_ν is the flux density at frequency ν, k_ν is the dust mass absorption coefficient, B is the Planck function ($B = \frac{2h\nu^3}{c^2}\frac{1}{e^{\frac{h\nu}{k_{\mathrm{B}}T}}-1}$), M_{du} is the dust mass, k_{B} is the Boltzmann constant and d is the distance to the SMC (60.6 kpc). The absorption coefficient is adopted from the SMC bar model of Weingartner and Draine (2001). The model consists of mixture of carbonaceous grains, and amorphous silicate grains. Carbonaceous grains are similar to polycyclic aromatic hydrocarbons when small, and graphite-like when large (Li and Draine, 2001). Using the size distribution from Weingartner and Draine (2001), absorption coefficients were calculated and compiled into a table[8].

Fluxes for LMC SNRs taken from Seok, Koo, and Onaka (2013) are recalculated for the distance of the SMC, and only fluxes where the entire remnant or entire shell was used as an extraction region were used. Assuming the proportionality $k_\nu \propto \nu^\beta$ with $\beta = 2$, lines of constant dust temperature can be constructed in the plane using the formula

$$F_{\nu_1} = F_{\nu_2} \times \frac{\nu_1^5}{\nu_2^5} \frac{e^{\frac{h\nu_2}{k_{\mathrm{B}}T_{\mathrm{du}}}} - 1}{e^{\frac{h\nu_1}{k_{\mathrm{B}}T_{\mathrm{du}}}} - 1} \tag{2}$$

These lines of constant dust temperature are shown as dashed lines in figure 15. Similarly, lines of constant dust mass are constructed calculating 2 points in the plane via the formula 1. These lines are dotted lines in figure 15.

The observed 24 and 70 μm fluxes can be explained by a temperature range of $43\,\mathrm{K} < T_{\mathrm{du}} < 57\,\mathrm{K}$ and a mass range of $0.002\,M_\odot < M_{\mathrm{du}} < 0.5\,M_\odot$. The temperature range is consistent with, yet narrower than that of SNRs analyzed in Seok, Koo, and Onaka (2013) ($T_{\mathrm{du}} \sim 45$ to $80\,\mathrm{K}$) or that in Galactic SNRs (between ~ 45 and $85\,\mathrm{K}$, Pinheiro Gonçalves et al., 2011).

The dust mass range is very similar to the range for the LMC ($M_{\mathrm{du}} \lesssim 0.001$ to $0.8\,M_\odot$) and slightly lower than the range for Galactic SNRs ($0.008\,M_\odot$ for Cas A to $2.5\,M_\odot$ for W44, Pinheiro Gonçalves et al., 2011).

---

[8]*Extinction, scattering and absorption properties computed for smc bar model.* URL: `ftp://ftp.astro.princeton.edu/draine/dust/mix/kext_albedo_WD_SMCbar_0` (Accessed: 10 Nov. 2018).
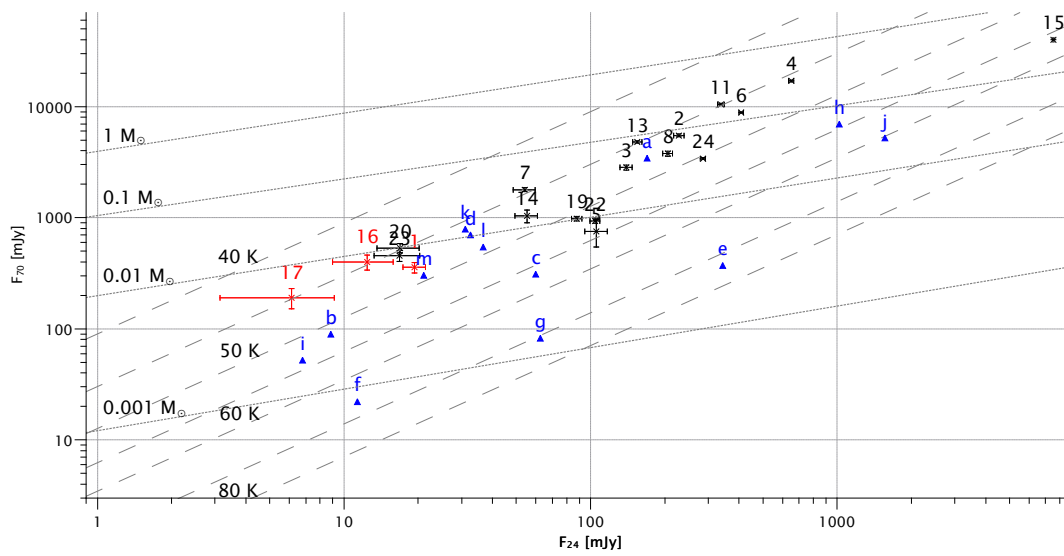
Figure 15: 70 μm flux vs. 24 μm flux of SMC SNRs (diagonal crosses with errorbars, indexed with numbers) and selected LMC SNRs (blue triangles, indexed with letters, from Seok, Koo, and Onaka, 2013). Red dots indicate SNRs with multiple negative IR fluxes. Dotted and dashed lines show a grid of constant dust masses and temperatures for blackbody emission.

index	name	$F_{3.6}$	$F_{4.5}$	$F_{5.8}$	F_8	F_{24}	F_{70}	F_{160}	F_{A65}	F_{A90}	F_{A140}	F_{A160}	size [as]
SMC SNRs
1	(J004055-733654)	0.1 ± 1.9	3.9 ± 1.7	3 ± 9	11 ± 4	19.4 ± 2.0	370 ± 40	540 ± 290	1010 ± 170	400 ± 160	80 ± 190	20 ± 190	174
2	J004637-730823	13.8 ± 2.5	11.5 ± 2.2	60 ± 7	118 ± 6	228 ± 11	5500 ± 160	10900 ± 800	6500 ± 600	7300 ± 600	11600 ± 700	9700 ± 800	111
3	J004716-730811	16.2 ± 2.2	14.7 ± 1.9	34 ± 6	31 ± 5	139 ± 9	2830 ± 140	1600 ± 500	3000 ± 400	1500 ± 400	1900 ± 500	900 ± 400	66
4	J004728-730601	56 ± 4	45 ± 4	70 ± 9	164 ± 8	651 ± 15	16970 ± 300	14100 ± 1300	14000 ± 700	11600 ± 900	16200 ± 1300	16800 ± 1200	165
5	J004741-730930	6.1 ± 2.2	7.5 ± 2.1	19 ± 6	31 ± 5	106 ± 11	750 ± 210	200 ± 600	1400 ± 600	800 ± 600	-200 ± 700	-3300 ± 500	90
6	J004821-731931	-3 ± 3	1.8 ± 1.3	7 ± 4	25 ± 4	54 ± 6	1790 ± 80	2100 ± 400	1120 ± 240	1490 ± 260	600 ± 500	-620 ± 240	111
8	J004907-731402	-10 ± 10	6.3 ± 2.2	45 ± 7	101 ± 6	206 ± 10	3770 ± 190	2200 ± 400	2600 ± 500	3400 ± 600	3200 ± 1000	5000 ± 800	121
9	(J005110-732212)	-8 ± 4	-2.6 ± 1.8	-9 ± 7	-6 ± 4	5 ± 5	20 ± 70	-100 ± 400	610 ± 180	70 ± 250	800 ± 400	1940 ± 280	175
10	(J005152-731034)	-1.8 ± 1.3	-1.2 ± 1.1	-3 ± 4	-2.1 ± 2.2	-2.0 ± 2.5	-110 ± 50	-120 ± 240	-50 ± 130	-130 ± 180	-310 ± 260	-350 ± 250	97
11	J005240-723820	12 ± 6	24 ± 4	42 ± 17	129 ± 9	338 ± 11	10480 ± 180	15700 ± 900	7900 ± 500	11700 ± 600	11600 ± 900	10200 ± 500	302
13	J005800-721101	10.6 ± 2.4	8.8 ± 2.1	27 ± 10	43 ± 5	155 ± 7	4780 ± 110	8500 ± 600	5300 ± 400	8400 ± 400	11200 ± 700	4100 ± 400	114
14	J005817-721814	18.5 ± 2.4	7.3 ± 2.0	20 ± 9	27 ± 5	55 ± 6	1040 ± 140	1700 ± 600	1000 ± 400	2300 ± 400	2800 ± 600	1100 ± 300	210
15	J005927-721010	124 ± 4	152 ± 5	270 ± 9	541 ± 9	7520 ± 40	40010 ± 240	36400 ± 700	48300 ± 700	40000 ± 800	41800 ± 700	19000 ± 500	181
16	(J010018-713341)	-0.4 ± 1.4	0.2 ± 1.2	-2 ± 9	13 ± 4	12 ± 4	400 ± 70	2100 ± 500	690 ± 200	1000 ± 400	600 ± 500	740 ± 250	137
17	(J010313-720958)	23.8 ± 1.8	22.9 ± 1.7	10 ± 4	6.3 ± 2.0	6.1 ± 3.0	190 ± 40	100 ± 180	210 ± 130	60 ± 140	10 ± 170	180 ± 130	86
18	(J010329-724728)	-0.3 ± 0.7	-0.4 ± 0.6	0 ± 4	0.8 ± 1.4	2.3 ± 0.6	42 ± 15	0 ± 110	150 ± 50	10 ± 70	30 ± 80	0 ± 70	86
19	J010402-720149	1.1 ± 0.8	1.0 ± 0.7	5.5 ± 2.9	12.5 ± 1.9	88 ± 5	980 ± 50	1140 ± 210	170 ± 140	900 ± 180	1450 ± 220	720 ± 160	60
20	J010505-722319	2.9 ± 1.5	2.5 ± 1.3	5 ± 8	6.4 ± 3.0	17 ± 4	530 ± 50	710 ± 280	-520 ± 180	130 ± 170	570 ± 240	730 ± 20	194
21	(J010524-720923)	-4.5 ± 1.7	-2.8 ± 1.4	-4 ± 8	-7 ± 4	-23 ± 5	-700 ± 110	-700 ± 500	350 ± 210	-300 ± 400	-400 ± 500	-1300 ± 500	149
22	J010541-720340	4.9 ± 1.0	3.7 ± 0.9	14 ± 4	30.9 ± 2.4	104 ± 5	940 ± 50	120 ± 240	600 ± 170	660 ± 180	650 ± 230	430 ± 200	79
23	J010619-720527	3.4 ± 1.1	6.7 ± 1.1	16 ± 5	12.8 ± 2.5	17 ± 4	460 ± 60	290 ± 270	310 ± 180	10 ± 220	0 ± 300	-280 ± 220	79
SMC SNR candidates
7	J0049.0-7306	23.9 ± 2.6	21.2 ± 2.3	106 ± 7	235 ± 7	409 ± 10	8860 ± 120	14400 ± 600	8800 ± 400	9400 ± 500	15200 ± 600	8900 ± 600	45
12	(J0056.5-7208)	0 ± 1.8	-0.4 ± 1.5	-2 ± 8	-4 ± 4	-9.7 ± 2.9	-980 ± 60	-1300 ± 400	-280 ± 170	-970 ± 200	-330 ± 280	-140 ± 190	103
24	J011333-731704	9.2 ± 1.1	11.3 ± 1.2	20 ± 4	43.2 ± 2.5	286 ± 7	3400 ± 70	4600 ± 400	4380 ± 250	5800 ± 400	6700 ± 400	4800 ± 400	76
LMC SNRs
a	0450-70.9	19.2 ± 0.21	18.4 ± 0.24	101 ± 0.96	250 ± 0.96	169 ± 3.2	3438 ± 43	-	-	-	-	-	296
b	N11L	0.77 ± 0.03	1.21 ± 0.03	2.79 ± 0.11	≤ 2.3	8.84 ± 0.51	89.8 ± 15	-	-	-	-	-	43.9
c	DEM L71	—	—	—	< 0.72	60.0 ± 6.0	309 ± 64	-	-	-	-	-	-
d	DEM L72	≤ 2.2	≤ 2.0	≤ 21	50.9 ± 0.47	32.6 ± 1.5	704 ± 21	-	-	-	-	-	149
e	N103B	≤ 5.1	≤ 3.1	≤ 28	≤ 78	343 ± 1.4	373 ± 19	-	-	-	-	-	29.9
f	0509-67.5	—	—	—	< 0.14	11.4 ± 1.2	< 22.2	-	-	-	-	-	-
g	0519-69.0	—	—	—	< 0.61	62.6 ± 6.3	< 82.3	-	-	-	-	-	-
h	N49	22	28	88	122	1020	6935	-	-	-	-	-	35.7
i	SNR in N206	2.28 ± 0.03	1.65 ± 0.04	10.9 ± 0.13	20.4 ± 0.2	16.7 ± 0.89	≤ 91	-	-	-	-	-	43.3
j	N63A	25	22	88	204	1564	5236	-	-	-	-	-	38.7
k	DEM L241	0.33 ± 0.10	5.15 ± 0.08	≤ 1.5	≤ 3.9	31.1 ± 9.6	≤ 785	-	-	-	-	-	23.9
l	DEM L249	4.15 ± 0.05	4.90 ± 0.04	32.0 ± 0.14	63.9 ± 0.27	36.7 ± 0.75	543 ± 28	-	-	-	-	-	87.1
m	DEM L316A	1.90 ± 0.03	4.15 ± 0.04	15.6 ± 0.13	≤ 9.5	21.1 ± 0.68	303 ± 18	-	-	-	-	-	57.4

Table 2: Fluxes of the analyzed SNRs at different wavelengths, all wavelengths in μm and all fluxes in mJy. Fluxes denoted with an A are from AKARI data. Index numbers are references for diagrams. Remnant names in brackets are marked/excluded remnants. Fluxes for LMC SNRs were taken from Seok, Koo, and Onaka (2013).

3.2 Comparison of IR and x-ray data

When comparing IR and x-ray morphologies of the SNRs, only 2 remnants have strong similarities, one of which is excluded due to negative background-substracted IR fluxes at most wavelengths. SNR J010402-720149 (more known under the name B0102-72.3, especially in x-ray analyses) shows a similar morphology at $24\,\mu$m when compared to x-ray images (see figure 11). Remnant J005240-723624 shows some features in IR images that are visible in x-ray images (figure 8). 11 other remnants show considerable discrepancies between IR and x-ray morphologies, the rest are too faint in either to distinguish morphologies. Due to the low number of remnants with similar morphologies, IR and x-ray fluxes have been compared across all remnants that were not previously excluded or have no x-ray data.

X-ray fluxes for remnants were estimated using the WebPIMMS tool[9] using the APEC model with 0.2 solar abundance, $kT = 0.68\,$keV, $nH = 4 \cdot 10^{21}\,$cm^{-2} and an energy range of $0.3 - 5$ keV (Yokogawa et al., 2000). Table 3 shows the values for x-ray flux and νF_{24}. Figure 16 shows νF_{24} over the estimated x-ray fluxes. A linear fit of the data did not return any significant correlation ($R^2 = 0.006732$).

SNRs with higher x-ray fluxes tend to have higher νF_{24}. This analysis was split up into two populations: Isolated SNRs and SNRs in direct vicinity of other SNRs, HII regions or stars. This was done to mitigate potential spillover effects when comparing isolated SNRs with others. SNRs J005927-721010 (index 15), J010402-720149 (index 19) and J010505-722319 (index 20) appear as outliers in figure 16, figure 17 shows them in $24\,\mu$m and x-ray. SNR J005927-721010 is very close to a star-forming region and star cluster NGC 346 (see figure 9 in section 2.5, index 4), which explains its high IR flux compared to x-ray. The star cluster is not visible in x-ray at all, but very bright at $24\,\mu$m, see subfigures a) and b) in figure 17.

The other two remnants are the two brightest x-ray SNRs in the SMC (Haberl et al., 2000) and both appear significantly higher in x-ray as well as lower in $24\,\mu$m than the rest of the analyzed remnants. Remnant J010402-720149's x-ray spectra have been studied in great depth in other works, revealing its oxygen-rich nature of $\approx 6\,M_\odot$ of oxygen (Flanagan et al., 2004) and nonequilibrium ionization conditions (Rasmussen, A. P. et al., 2001).

Remnant J010505-722319 is of substantial size, being the third largest SNR in the SMC (see table 2). Radio and x-ray studies of this remnant have revealed overabundances of O and Ne (Yokogawa et al., 2002 and Park et al., 2003) in the center spectrum, as well as Ne in the integrated spectrum (Takeuchi, Yamaguchi, and Tamagawa, 2016). It is also classified as an oxygen-rich SNR. Remnants J010402-720149 and J010505-722319 are the only two of this class in the SMC.

---

[9] *WebPIMMS tool*. URL: https://heasarc.gsfc.nasa.gov/cgi-bin/Tools/w3pimms/w3pimms.pl (Accessed: 10 Nov. 2018).

| index	name	$\nu F_{24}[10^{-12}\frac{\text{erg}}{\text{cm}^2\text{s}}]$	x-ray flux $[10^{-12}\frac{\text{erg}}{\text{cm}^2\text{s}}]$	figure in section 2.5
2	J004637-730823	2.85 ± 0.14	0.194 ± 0.015	3
3	J004716-730811	1.74 ± 0.11	0.074 ± 0.011	3
4	J004728-730601	8.14 ± 0.19	0.335 ± 0.018	3
5	J004741-730930	1.32 ± 0.14	0.418 ± 0.017	3
6	J004821-731931	0.68 ± 0.07	0.068 ± 0.009	4
7	J0049.0-7306	2.57 ± 0.12	0.029 ± 0.007	3
11	J005240-723624	4.22 ± 0.14	0.164 ± 0.011	8
13	J005800-721101	1.93 ± 0.09	0.030 ± 0.006	9
14	J005817-721814	0.69 ± 0.08	0.112 ± 0.009	9
15	J005927-721010	93.9 ± 0.5	0.644 ± 0.020	9
19	J010402-720149	1.10 ± 0.06	25.17 ± 0.23	11
20	J010505-722319	0.21 ± 0.05	3.51 ± 0.06	13
22	J010541-720340	1.30 ± 0.06	0.045 ± 0.007	11
23	J010619-720527	0.21 ± 0.05	0.377 ± 0.017	11

Table 3: Comparison of fluxes at 24 µm with x-ray fluxes.
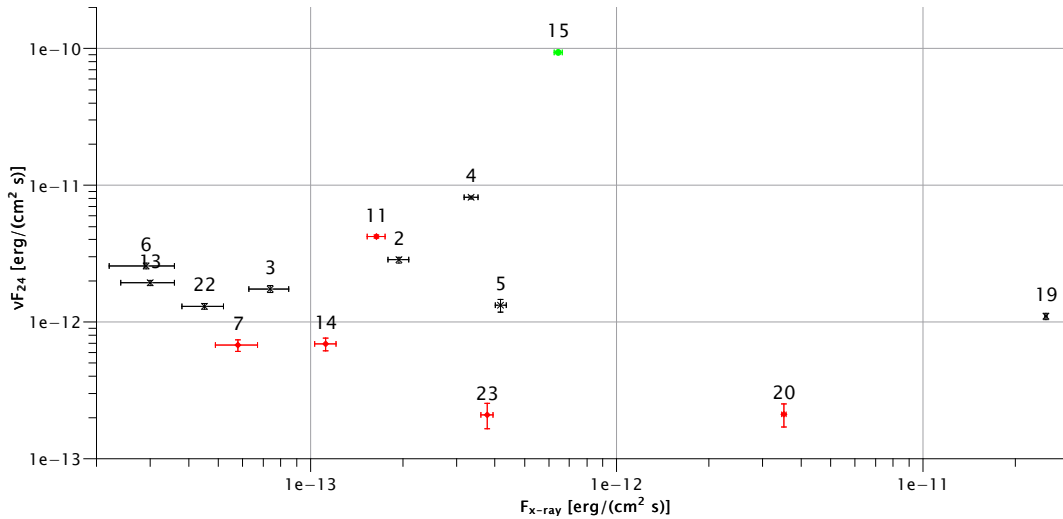
Figure 16: νF_{24} over x-ray flux of analyzed SNRs. Red diamonds with red errorbars indicate isolated remnants. Green circle is SNR J005927-721010, which is close to star-forming region and cluster NGC 346.
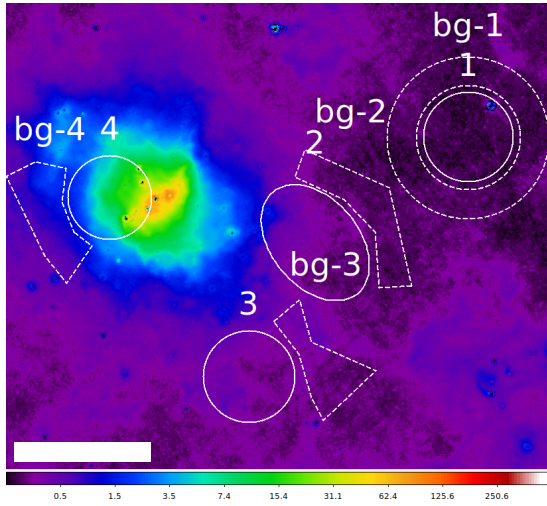
(a) J005927-721010-24 μm
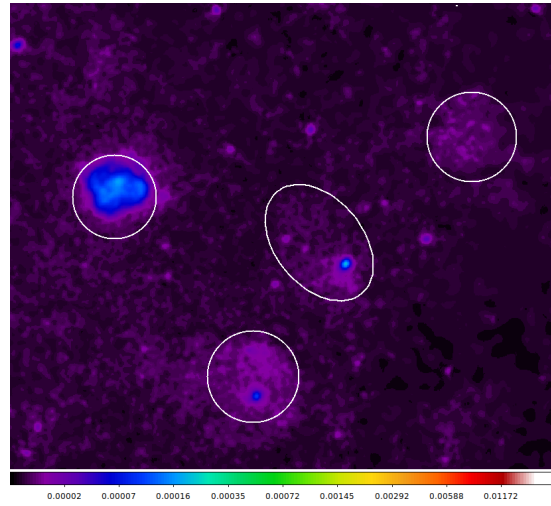
(b) J005927-721010-x-ray

(c) J010402-720149-24 μm
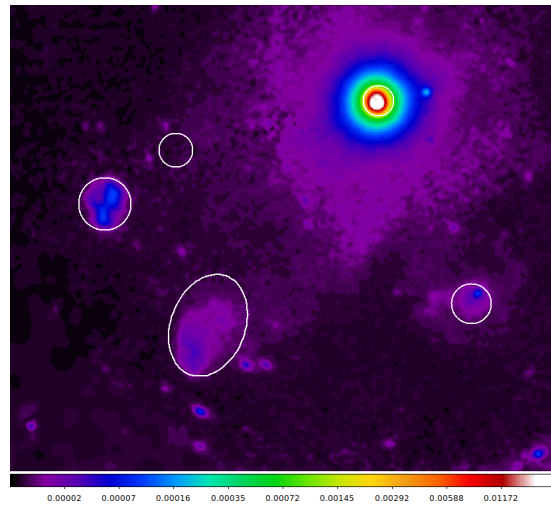
(d) J010402-720149-x-ray
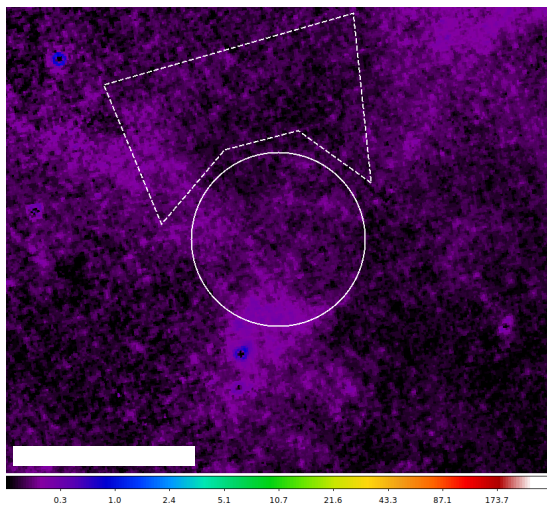
(e) J010505-722319-24 μm
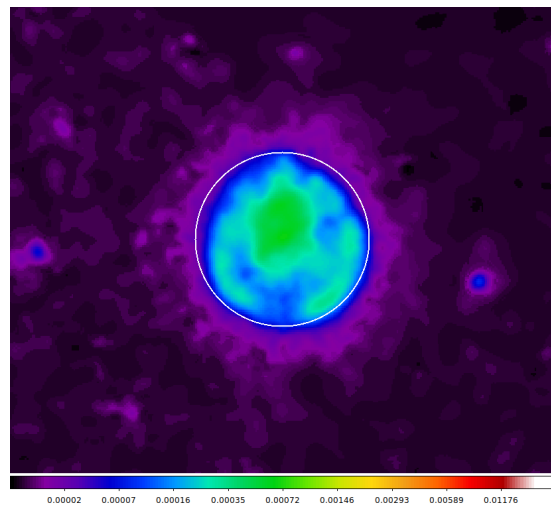
(f) J010505-722319-x-ray

Figure 17: SNRs J005927-721010 with index 4 in subfigures a) and b), J010402-720149 with index 2 in c) and d) and J010505-722319 in e) and f) in 24 μm and x-ray, respectively.

3.3 Comparison of IR flux to SNR size

Using the data as presented in table 2, the IR flux at 24 μm is compared to the size of the SNRs. SNRs with larger extent tend to have higher 24 μm-fluxes. The analysis was again
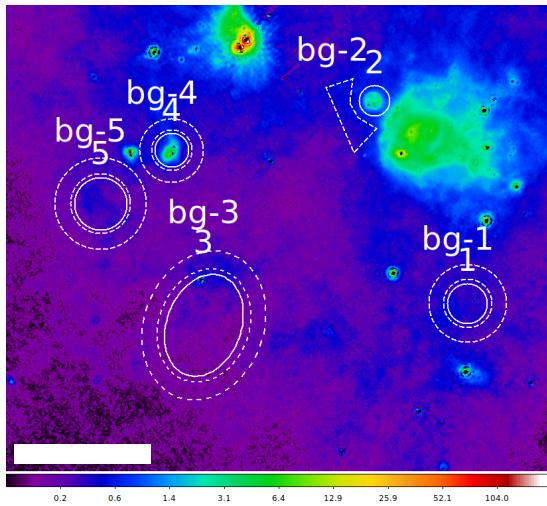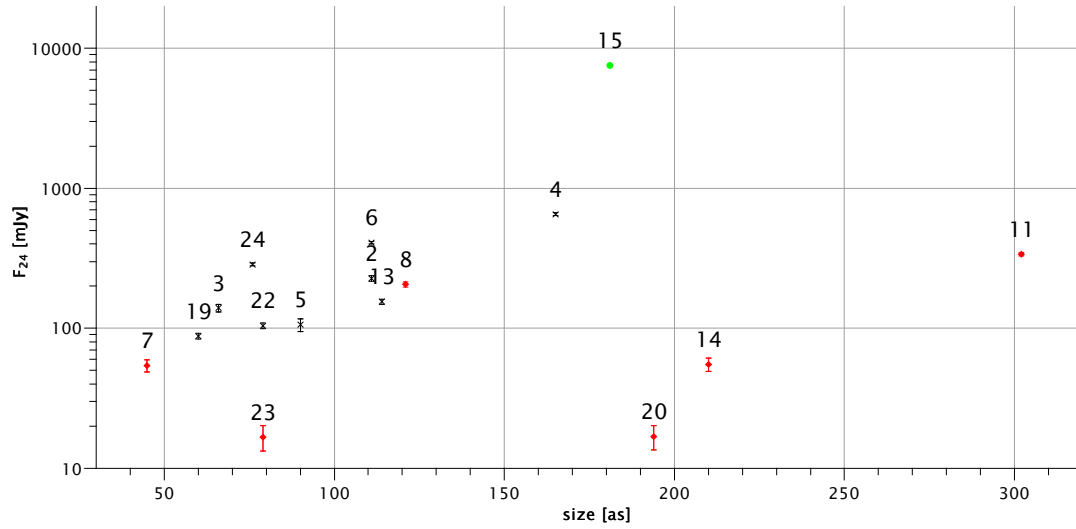

Figure 18: F_{24} over size in as of analyzed SNRs. Red diamonds with red errorbars indicate isolated remnants. Green circle is SNR J005927-721010, which is close to star-forming region and cluster NGC 346.

split into isolated remnants and remnants embedded in HII regions or in direct vicinity of other SNRs, HII regions, or stars for the same reason as in section 3.2. The only outlier with respect to those two populations is SNR J005927-721010, which is again close to a star-forming region and cluster NGC 346, which explains its relatively higher F_{24}.

4 Discussion

IR properties of SNRs in the SMC were studied using archival Spitzer data from IRAC and MIPS instruments. The detected IR emission was in part compared to x-ray data to start adding IR emission to the multiwavelength analysis of SNRs in the SMC.

Out of 21 SNRs and 3 candidates, 14 and 2 show detectable IR emission in IRAC (3.6, 4.5, 5.8 and 8 μm) and/or MIPS (24, 70 and 160 μm) as well as some AKARI (65, 90, 140 and 160 μm) bands. IR morphologies for all 24 SNRs and candidates are shown in this paper at all IRAC and MIPS wavelengths alongside a RGB image of optical emission lines as well as a x-ray image. The morphologies of 8 remnants were similar in IR and optical images, for 2 remnants were they similar in IR and x-ray images. The detection rate of ∼ 67% is substantially higher than that of Galactic SNRs (∼ 30%). It is very similar to the detection rate of LMC SNRs reported in Seok, Koo, and Onaka (2013) at ∼ 62%. The major reason is therefore likely the same as for the LMC, less IR confusion by the Galactic disk.

Assuming mid-infrared emission to be dominated by dust grains in thermal equilibrium, observed 24 and 70 μm fluxes can be compared to a modified blackbody spectrum (equation 1). This comparison produces constraints on the dust mass and temperature of the SMC SNRs.

The dust mass derived from this lies between 0.002 and 0.5 $M_\odot$, which is very close to the range reported for LMC SNRs in Seok, Koo, and Onaka (2013) of 0.001 to 0.8 $M_\odot$. It is lower than the range reported for Galactic SNRs in Pinheiro Gonçalves et al. (2011) of 0.02 to 2.5 $M_\odot$.

The dust temperature of the simulated blackbody spectrum that fits the observed data lies between 43 and 57 K. This range is somewhat narrower than the range for LMC (45 to 80 K, Seok, Koo, and Onaka, 2013) or Galactic SNRs (45 to 70 K, Pinheiro Gonçalves et al., 2011), as well as slightly lower.

Both in the comparison between IR flux and SNR size as well as between 24 μm flux and x-ray flux, the remnants were split into two groups. Isolated remnants and remnants close to other objects bright in IR (for example other SNRs or large bodies of interstellar dust) were analyzed separately. Within these two groups separately, a correlation between remnant size and IR flux at 24 μm was found. Since SNR size increases with age, this points towards most of the IR flux coming from shocked and heated interstellar dust rather than from dust produced in the ejecta. IR emission dominated by ejecta-produced dust would stagnate after a few hundred years.

From comparing the IR flux at 24 μm to x-ray flux separately for isolated remnants and remnants close to other IR-bright objects, a positive correlation between the two was found. The outliers to this correlation are SNRs J005927-721010, J010402-720149 and J010505-722319. J005927-721010 is close to a star-forming region and star cluster, explaining its relatively higher IR flux. J010402-720149 and J010505-722319 are the only two oxygen-rich SNRs in the SMC, which is a possible reason for their relatively lower IR flux. They are also both among the largest SNRs in the SMC.

Lastly, SNRs in IR-bright regions being brighter than isolated SNRs (see figures 16 and 18, red diamonds being isolated SNRs) either points towards the background substraction not being sufficient or higher amounts of dust in the vicinity of SNRs in IR-bright regions being heated up and emitting at 24 μm.

5 Outlook

Similarly to the LMC, the SMC contains SNRs at better viewing angles with regards to IR confusion by the Galactic disc than our own galaxy. A morphological study of SNRs in the SMC as well as more comparisons to multiwavelength data could further the conclusions that can be drawn about the SNRs from IR emission. Of special interest would be comparisons between IR and x-ray for J010402-720149 and J010505-722319 to find the reason for their relatively low IR flux compared to their very high x-ray fluxes. A multiwavelength morphological study of J005800-721101 with potentially higher resolution data in the future could reveal whether there are multiple remnants visible at different wavelengths at its position or if it is different parts of the same remnant.

References

AKARI. URL: http://www.ir.isas.jaxa.jp/AKARI/Observation/ (Accessed: 10 Nov. 2018).

Arendt, R. G. (May 1989). "An infrared survey of Galactic supernova remnants". In: \apjs 70, pp. 181–212. DOI: 10.1086/191337.

Badenes, Carles, Dan Maoz, and Bruce T. Draine (2010). "On the size distribution of supernova remnants in the Magellanic Clouds". In: *Monthly Notices of the Royal Astronomical Society* 407.2, pp. 1301–1313. DOI: 10.1111/j.1365-2966.2010.17023.x. URL: http://dx.doi.org/10.1111/j.1365-2966.2010.17023.x.

Douvion, T., P. O. Lagage, and E. Pantin (Apr. 2001). "Cassiopeia A dust composition and heating". In: \aap 369, pp. 589–593. DOI: 10.1051/0004-6361:20010053.

Douvion, T. et al. (July 2001). "Dust in the Tycho, Kepler and Crab supernova remnants". In: \aap 373, pp. 281–291. DOI: 10.1051/0004-6361:20010447.

Extinction, scattering and absorption properties computed for smc bar model. URL: ftp://ftp.astro.princeton.edu/draine/dust/mix/kext_albedo_WD_SMCbar_0 (Accessed: 10 Nov. 2018).

Filipović, M. D. et al. (2005). "An ATCA radio-continuum study of the Small Magellanic Cloud — III. Supernova remnants and their environments". In: *Monthly Notices of the Royal Astronomical Society* 364.1, pp. 217–236. DOI: 10.1111/j.1365-2966.2005.09554.x. URL: http://dx.doi.org/10.1111/j.1365-2966.2005.09554.x.

Flanagan, K. A. et al. (2004). "Chandra High-Resolution X-Ray Spectrum of Supernova Remnant 1E 0102.2–7219". In: *The Astrophysical Journal* 605.1, p. 230. URL: http://stacks.iop.org/0004-637X/605/i=1/a=230.

Gordon, K. D. et al. (Oct. 2011). "Surveying the Agents of Galaxy Evolution in the Tidally Stripped, Low Metallicity Small Magellanic Cloud (SAGE-SMC). I. Overview". In: \aj 142, p. 102. DOI: 10.1088/0004-6256/142/4/102.

Haberl, F. et al. (2000). "A ROSAT PSPC catalogue of X-ray sources in the SMC region*". In: *Astron. Astrophys. Suppl. Ser.* 142.1, pp. 41–57. DOI: 10.1051/aas:2000136. URL: https://doi.org/10.1051/aas:2000136.

Haberl, F. et al. (2012). "The XMM-Newton survey of the Small Magellanic Cloud". In: *A&A* 545, A128. DOI: 10.1051/0004-6361/201219758. URL: https://doi.org/10.1051/0004-6361/201219758.

Heyden, K. J. van der, J. A. Bleeker, and J.S. Kasstra (Mar. 2004). "Synoptic study of the SMC SNRs using XMM-Newton". In: \aap 421, pp. 1031–1043. DOI: 10.1051/0004-6361:20034156.

Infrared Astronomical Satellite. URL: https://irsa.ipac.caltech.edu/Missions/iras.html (Accessed: 10 Nov. 2018).

Infrared Space Observatory. URL: https://www.cosmos.esa.int/web/iso (Accessed: 10 Nov. 2018).

Koo, Bon-Chul et al. (2007). "AKARI Detection of the Infrared-Bright Supernova Remnant B0104$-$72.3 in the Small Magellanic Cloud". In: *Publications of the Astronomical Society of Japan* 59 (sp2), S455–S461. DOI: 10.1093/pasj/59.sp2.S455. URL: http://dx.doi.org/10.1093/pasj/59.sp2.S455.

Li, Aigen and B. T. Draine (2001). "Infrared Emission from Interstellar Dust. II. The Diffuse Interstellar Medium". In: *The Astrophysical Journal* 554.2, p. 778. URL: http://stacks.iop.org/0004-637X/554/i=2/a=778.

Mathewson, D. S. et al. (June 1984). "Supernova remnants in the Magellanic Clouds". In: \apjs 55, pp. 189–210. DOI: 10.1086/190952.

Park, Sangwook et al. (2003). "0103–72.6: A New Oxygen-rich Supernova Remnant in the Small Magellanic Cloud". In: *The Astrophysical Journal Letters* 598.2, p. L95. URL: http://stacks.iop.org/1538-4357/598/i=2/a=L95.

Pinheiro Gonçalves, D. et al. (Aug. 2011). "The MIPSGAL View of Supernova Remnants in the Galactic Plane". In: \aj 142, p. 47. DOI: 10.1088/0004-6256/142/2/47.

Rasmussen, A. P. et al. (2001). "The X-ray spectrum of the supernova remnant 1E 0102.2-7219". In: *A&A* 365.1, pp. L231–L236. DOI: 10.1051/0004-6361:20000231. URL: https://doi.org/10.1051/0004-6361:20000231.

ROSAT PSPC source catalogue. URL: http://vizier.u-strasbg.fr/viz-bin/VizieR?-source=J/A+AS/142/41 (Accessed: 10 Nov. 2018).

Saken, J. M., R. A. Fesen, and J. M. Shull (Aug. 1992). "An IRAS survey of Galactic supernova remnants". In: \apjs 81, pp. 715–745. DOI: 10.1086/191703.

Seok, Ji Yeon, Bon-Chul Koo, and Takashi Onaka (2013). "A Survey of Infrared Supernova Remnants in the Large Magellanic Cloud". In: *The Astrophysical Journal* 779.2, p. 134. URL: http://stacks.iop.org/0004-637X/779/i=2/a=134.

Spitzer Heritage Archive. URL: https://sha.ipac.caltech.edu/applications/Spitzer/SHA/ (Accessed: 10 Nov. 2018).

Spitzer Space Telescope. URL: http://www.spitzer.caltech.edu/ (Accessed: 10 Nov. 2018).

Takeuchi, Yoko, Hiroya Yamaguchi, and Toru Tamagawa (2016). "A systematic study of evolved supernova remnants in the large and small Magellanic Clouds with Suzaku". In: *Publications of the Astronomical Society of Japan* 68 (SP1), S9. DOI: 10.1093/pasj/psv127. URL: http://dx.doi.org/10.1093/pasj/psv127.

WebPIMMS tool. URL: https://heasarc.gsfc.nasa.gov/cgi-bin/Tools/w3pimms/w3pimms.pl (Accessed: 10 Nov. 2018).

Weingartner, Joseph C. and B. T. Draine (2001). "Dust Grain-Size Distributions and Extinction in the Milky Way, Large Magellanic Cloud, and Small Magellanic Cloud". In: *The Astrophysical Journal* 548.1, p. 296. URL: http://stacks.iop.org/0004-637X/548/i=1/a=296.

Yokogawa, Jun et al. (2000). "A Study of the Populations of X-Ray Sources in the Small Magellanic Cloud with ASCA". In: *The Astrophysical Journal Supplement Series* 128.2, p. 491. URL: http://stacks.iop.org/0067-0049/128/i=2/a=491.

Yokogawa, Jun et al. (2002). "Centrally Peaked X-Ray Supernova Remnants in the Small Magellanic Cloud Studied with ASCA and ROSAT". In: *Publications of the Astronomical Society of Japan* 54.1, pp. 53–59. DOI: 10.1093/pasj/54.1.53. URL: http://dx.doi.org/10.1093/pasj/54.1.53.

Appendices

A   Source code of *calculatefluxalltypes.pro*

```
; This IDL routine is for computing fluxes from a FITS file
    ↪ using
; two ds9 region files: one for the sources and one for the
    ↪ background
; regions. They should be in two different files, in the same
    ↪ order, and
; both in image coordinates.

; NOTE: uses functions from the NASA IDLastro package, and also
; ds9sourcepars.pro, inside.pro, and aperisherr.pro.



;
    ↪
; READS A FITS FILE AND TWO REGION FILES (ONE FOR SOURCES AND
    ↪ ONE FOR
; THE ACCOMPANYING BACKGROUNDS), THEN CALCULATES THE FLUX

; read the cutout file data and header
;fitsdata = READFITS('/userdata/data/ingenhuett/
    ↪ cutoutscriptoutput/MIPS160_cutout.fits', fitsheader)
fitsdata = READFITS('/userdata/data/ingenhuett/fullsize images/
    ↪ l313.52_b-65.00_ecl_6deg_N160_fixstripe.fits', fitsheader)
fitssizex = SXPAR(fitsheader, 'NAXIS1')
fitssizey = SXPAR(fitsheader, 'NAXIS2')
;pxscale = SXPAR(fitsheader, 'PLTSCALE')
;pxcale for AKARI files is 15 arcsec, header only contains a
    ↪ number rounded in degrees
pxscale = 15

; location of the source region file (!! use image coordinates
    ↪ !!)
sourcefile = '/userdata/data/ingenhuett/cutoutscriptoutput/
    ↪ AKARI160sources.reg'

; location of the background region file (!! image coordinates
    ↪ !!)
; in same order as the sources!!
bgfile = '/userdata/data/ingenhuett/cutoutscriptoutput/
    ↪ AKARI160bg.reg'

; read the source region file lines as string into an array "
```

```
      ↪ reginfo"
READCOL, sourcefile, F='A', reginfo, skipline=3, delimiter=' ';,
   ↪  comment='#'
print, 'Extracting the source regions.'
lkm_apers = SIZE(reginfo, /N_ELEMENTS)


; read the background file (assumes all regions are polygons)
READCOL, bgfile, F='A', bginfo, skipline=3, delimiter=' ',
   ↪ comment='#'
print, 'Extracting the background regions.'


; for diagnostic purposes, save the system time into a variable
t1=systime(0,/sec)


; open a file to store the fluxes and errors in
openw, unit1, '/userdata/data/ingenhuett/cutoutscriptoutput/160
   ↪ fluxesA.dat', /get_lun, width = 200
; write a header for the file
printf, unit1, FORMAT='("Source number ", 2X, "total flux[mJy]",
   ↪  2X, "error", 11X, "size[sr]", 8X)'
printf, unit1,
   ↪ '===========================================================',
   ↪
; format template for data writing
; printf, unit1, FORMAT='(I2,14X,F14.10,2X,F14.10,2X,F14.10)'



; go through each aperture in the region file
FOR s=0, lkm_apers-1 DO BEGIN
;lkm_apers-1

; ANALYZE THE SOURCE REGION
    ; reformatting the ds9 source regions from a long string to
       ↪ an array
    ; ds9sourcepars is written for this
    sourceparams = ds9sourcepars(reginfo[s])
    regidents = SIZE(sourceparams, /N_ELEMENTS)
    CASE regidents OF
    3: BEGIN
        cenx = sourceparams[0]
    ceny = sourceparams[1]
    aperad = sourceparams[2]
    print, 'Region ', s+1
    print, 'Center x: ', cenx, ' Center y: ', ceny, ' Radius: ',
       ↪  aperad

    ; output is in IDL coordinates so 0 is the first pixel and
```

```
                  ↪ the
; integer values are in the pixel center like in ds9
cenx = cenx −1.0
ceny = ceny −1.0

; compute distances from a given pixel into array named
    ↪ givenape
dist_circle , givenape , [ fitssizex , fitssizey ] , uint(cenx) ,
    ↪ uint(ceny)

; find pixels that are inside the aperture radius and store
    ↪ them
; into an array regpixels
regpixels = where((givenape LT aperad) , pxcnt)

; regpixels contains array indices and can be used to locate
    ↪ those
; pixels in the data array
totalflux = TOTAL( fitsdata [ regpixels ])
meanflux = MEAN( fitsdata [ regpixels ])
print , 'Flux: ', totalflux , ', mean: ', meanflux , ', pixels:
    ↪ ', pxcnt

; 10 sigma correction
regvar = VARIANCE( fitsdata [ regpixels ])
tensigma = meanflux + (10 ∗ sqrt(regvar))
mintensigma = meanflux − (10 ∗ sqrt(regvar))
; print , tensigma
regpixelsa = where((givenape LT aperad) AND ( fitsdata lt
    ↪ tensigma) AND ( fitsdata gt mintensigma) , pxcnt)
fitsdataregpixels = fitsdata [ regpixelsa ]
regpixelsb = where((givenape LT aperad) AND (( fitsdata gt
    ↪ tensigma) OR ( fitsdata lt mintensigma)) ,
    ↪ pxcntsubstracted)
print , 'Excluding pixels over 10 sigma above the mean and
    ↪ below 0...'
print , 'Excluded ', pxcntsubstracted , ' pixels with values:
    ↪ ', fitsdata [ regpixelsb ]
; regpixelssubstracted = where(( fitsdata [ regpixelsa ] gt
    ↪ tensigma) , pxcntsubstracted)
totalflux = TOTAL( fitsdata [ regpixelsa ])
meanflux = MEAN( fitsdata [ regpixelsa ])
; print , 'Excluded pixels with values: ', fitsdata [
    ↪ regpixelssubstracted ]
print , 'Flux excluding those pixels: ', totalflux , ', mean:
    ↪ ', meanflux , ', pixels: ', pxcnt

END
```

```
5: BEGIN
    ellcenx = sourceparams[0]
ellceny = sourceparams[1]
ellaperad = sourceparams[4]
ellratio = sourceparams[2]
ellangle = sourceparams[3]
print, 'Region ', s+1
print, 'Center x: ', ellcenx, ' Center y: ', ellceny, '
  ↪ Major axis: ', ellaperad, ' Axis ratio: ', ellratio, '
  ↪  Angle: ', ellangle

; output is in IDL coordinates so 0 is the first pixel and
  ↪ the
; integer values are in the pixel center like in ds9
ellcenx = ellcenx −1.0
ellceny = ellceny −1.0

; compute distances from a given pixel into array named
  ↪ givenape
dist_ellipse, givenell, [fitssizex, fitssizey], uint(ellcenx
  ↪ ), uint(ellceny), ellratio, ellangle

; find pixels that are inside the aperture radius and store
  ↪ them
; into an array regpixels
regpixels = where((givenell LT ellaperad), pxcnt)

; regpixels contains array indices and can be used to locate
  ↪  those
; pixels in the data array
totalflux = TOTAL(fitsdata[regpixels])
meanflux = MEAN(fitsdata[regpixels])
print, 'Flux: ', totalflux, ', mean: ', meanflux, ', pixels:
  ↪  ', pxcnt


; 10 sigma correction
regvar = VARIANCE(fitsdata[regpixels])
elltensigma = meanflux + (10 * sqrt(regvar))
ellmintensigma = meanflux − (10 * sqrt(regvar))

;print, tensigma
regpixelsa = where((givenell LT ellaperad) AND (fitsdata lt
  ↪ elltensigma) AND (fitsdata gt ellmintensigma), pxcnt)
fitsdataregpixels = fitsdata[regpixelsa]
regpixelsb = where((givenell LT ellaperad) AND ((fitsdata gt
  ↪  elltensigma) OR (fitsdata lt ellmintensigma)),
  ↪ pxcntsubstracted)
```

```
        print , 'Excluding pixels over 10 sigma above the mean and
           ↪ below 0...'
        print , 'Excluded ', pxcntsubstracted , ' pixels with values:
           ↪ ', fitsdata [regpixelsb]
        ;regpixelssubstracted = where(( fitsdata [regpixelsa] gt
           ↪ tensigma ), pxcntsubstracted )
        totalflux = TOTAL( fitsdata [regpixelsa ])
        meanflux = MEAN( fitsdata [regpixelsa ])
        ;print , 'Excluded pixels with values: ', fitsdata [
           ↪ regpixelssubstracted ]
        print , 'Flux excluding those pixels: ', totalflux , ', mean:
           ↪ ', meanflux , ', pixels: ', pxcnt

           END
           ELSE: print , 'Source region ', s+1, ' was misinterpreted
              ↪ .'
           ENDCASE

; ANALYZE THE BACKGROUND REGION
        bgparams = ds9sourcepars ( bginfo [s])
        regidentbg = SIZE( bgparams , /N_ELEMENTS)
        CASE regidentbg OF
        4: BEGIN
        anncenx = bgparams [0]
        annceny = bgparams [1]
        annaperadinner = bgparams [2]
        annaperadouter = bgparams [3]
        print , 'Background for region ', s+1
        print , 'Center x: ', anncenx , ' Center y: ', annceny , '
           ↪ Inner radius: ', annaperadinner , ' Outer radius: ',
           ↪ annaperadouter

        ; output is in IDL coordinates so 0 is the first pixel and
           ↪ the
        ; integer values are in the pixel center like in ds9
        anncenx = anncenx −1.0
        annceny = annceny −1.0

        ; compute distances from a given pixel into array named
           ↪ givenape
        dist_circle , givenann , [ fitssizex , fitssizey ], uint ( anncenx)
           ↪ , uint ( annceny )

        ; find pixels that are inside the annullus and store them
        ; into an array annpixels
        annpixels = where (( givenann GT annaperadinner ) AND ( givenann
           ↪  LT annaperadouter ), annpxcnt )
```

```
; annpixels contains array indices and can be used to locate
    ↪   those
; pixels in the data array
anntotal = TOTAL(fitsdata[annpixels])
annmean = MEAN(fitsdata[annpixels])
annvar = VARIANCE(fitsdata[annpixels])
bgsubannflux = totalflux − pxcnt * annmean
bgsubannfluxmean = bgsubannflux / pxcnt
print, 'Annullus mean flux: ', annmean, ', pixels: ',
    ↪   annpxcnt

 ; compute the total error using the annullus
totalerrann = aperisherr(meanflux, pxcnt, annvar, annpxcnt)

; compute the source region size in sr (image in MJy/sr)
; 1 sq. arcsec = 2.3504*10^−11 sr
pxareasr = 2.3504e−11 * pxscale^2
regsizesr = pxareasr * pxcnt
print, 'Bkg−subtracted total flux [Jy]: ', bgsubannfluxmean
    ↪   * regsizesr * 1e6, ', error: ', totalerrann *
    ↪   regsizesr  * 1e6 / pxcnt

;10−sigma correction
anntensigma = annmean + (10 * sqrt(annvar))
annmintensigma = annmean − (10 * sqrt(annvar))
annpixelsa = where((givenann GT annaperadinner) AND (
    ↪   givenann LT annaperadouter) AND (fitsdata lt
    ↪   anntensigma) AND (fitsdata gt annmintensigma),
    ↪   annpxcnt)
annpixelsb = where((givenann GT annaperadinner) AND (
    ↪   givenann LT annaperadouter) AND ((fitsdata gt
    ↪   anntensigma) OR (fitsdata lt annmintensigma)),
    ↪   annpxcntb)
anntotal = TOTAL(fitsdata[annpixelsa])
annmean = MEAN(fitsdata[annpixelsa])
annvar = VARIANCE(fitsdata[annpixelsa])
bgsubannflux = totalflux − pxcnt * annmean
bgsubannfluxmean = bgsubannflux / pxcnt
print, 'Excluded ', annpxcntb, ' pixels in annullus with
    ↪   values', fitsdata[annpixelsb]
print, 'Annullus mean flux: ', annmean, ', pixels: ',
    ↪   annpxcnt

 ; compute the total error using the annullus
totalerrann = aperisherr(meanflux, pxcnt, annvar, annpxcnt)
    errannmean = totalerrann / pxcnt
; compute the source region size in sr (image in MJy/sr)
; 1 sq. arcsec = 2.3504*10^−11 sr
```

```
pxareasr = 2.3504e-11 * pxscale^2
regsizesr = pxareasr * pxcnt
print, 'Bkg-subtracted total flux [mJy]: ', bgsubannfluxmean
  ↪ * regsizesr * 1e9, ', error: ', errannmean *
  ↪ regsizesr * 1e9
writeflux = bgsubannfluxmean * regsizesr * 1e9
writeerr = errannmean * regsizesr * 1e9
printf, unit1, FORMAT='(I2,14X,F14.8,2X,F14.9,2X,F14.12)', s
  ↪ +1, writeflux, writeerr, regsizesr

;print, meanflux, regvar, annmean, annvar
    END
    6: BEGIN
    ellanncenx = bgparams[0]
ellannceny = bgparams[1]
ellannaperadinner = bgparams[4]
ellannaperadouter = bgparams[5]
ellannratio = bgparams[2]
ellannangle = bgparams[3]
print, 'Background for region ', s+1
print, 'Center x: ', ellanncenx, ' Center y: ', ellannceny,
  ↪ ' Inner major axis: ', ellannaperadinner, ' Outer
  ↪ major axis: ', ellannaperadouter, ' Axis ratio: ',
  ↪ ellannratio, ' Angle: ', ellannangle

; output is in IDL coordinates so 0 is the first pixel and
  ↪ the
; integer values are in the pixel center like in ds9
ellanncenx = ellanncenx-1.0
ellannceny = ellannceny-1.0

; compute distances from a given pixel into array named
  ↪ givenape
dist_ellipse, givenellann, [fitssizex, fitssizey], uint(
  ↪ ellanncenx), uint(ellannceny), ellannratio,
  ↪ ellannangle

; find pixels that are inside the annullus and store them
; into an array annpixels
ellannpixels = where((givenellann GT ellannaperadinner) AND
  ↪ (givenellann LT ellannaperadouter), ellannpxcnt)

; annpixels contains array indices and can be used to locate
  ↪ those
; pixels in the data array
ellanntotal = TOTAL(fitsdata[ellannpixels])
ellannmean = MEAN(fitsdata[ellannpixels])
ellannvar = VARIANCE(fitsdata[ellannpixels])
```

```
bgsubellannflux = totalflux − pxcnt ∗ ellannmean
bgsubellannfluxmean = bgsubellannflux / pxcnt
print, 'Annullus mean flux: ', ellannmean, ', pixels: ',
    ↪ ellannpxcnt

 ; compute the total error using the annullus
totalerrellann = aperisherr(meanflux, pxcnt, ellannvar,
    ↪ ellannpxcnt)

; compute the source region size in sr (image in MJy/sr)
; 1 sq. arcsec = 2.3504∗10^−11 sr
pxareasr = 2.3504e−11 ∗ pxscale^2
regsizesr = pxareasr ∗ pxcnt
print, 'Bkg−subtracted total flux [Jy]: ',
    ↪ bgsubellannfluxmean ∗ regsizesr ∗ 1e6, ', error: ',
    ↪ totalerrellann ∗ regsizesr ∗ 1e6 / pxcnt

;10−sigma correction
ellanntensigma = ellannmean + (10 ∗ sqrt(ellannvar))
ellannmintensigma = ellannmean − (10 ∗ sqrt(ellannvar))

ellannpixelsa = where((givenellann GT ellannaperadinner) AND
    ↪  (givenellann LT ellannaperadouter) AND (fitsdata lt
    ↪ ellanntensigma) AND (fitsdata gt ellannmintensigma),
    ↪ ellannpxcnt)
ellannpixelsb = where((givenellann GT ellannaperadinner) AND
    ↪  (givenellann LT ellannaperadouter) AND ((fitsdata gt
    ↪ ellanntensigma) OR (fitsdata lt ellannmintensigma)),
    ↪ ellannpxcntb)
ellanntotal = TOTAL(fitsdata[ellannpixelsa])
ellannmean = MEAN(fitsdata[ellannpixelsa])
ellannvar = VARIANCE(fitsdata[ellannpixelsa])
bgsubellannflux = totalflux − pxcnt ∗ ellannmean
bgsubellannfluxmean = bgsubellannflux / pxcnt
print, 'Excluded ', ellannpxcntb, ' pixels in annullus.'
print, 'Annullus mean flux: ', ellannmean, ', pixels: ',
    ↪ ellannpxcnt

 ; compute the total error using the annullus
totalerrellann = aperisherr(meanflux, pxcnt, ellannvar,
    ↪ ellannpxcnt)
    errellannmean = totalerrellann / pxcnt
; compute the source region size in sr (image in MJy/sr)
; 1 sq. arcsec = 2.3504∗10^−11 sr
pxareasr = 2.3504e−11 ∗ pxscale^2
regsizesr = pxareasr ∗ pxcnt
print, 'Bkg−subtracted total flux [mJy]: ',
    ↪ bgsubellannfluxmean ∗ regsizesr ∗ 1e9, ', error: ',
```

```
            ↪ errellannmean * regsizesr  * 1e9
writeflux = bgsubellannfluxmean * regsizesr * 1e9
writeerr = errellannmean * regsizesr  * 1e9
printf, unit1, FORMAT='(I2,14X,F14.8,2X,F14.9,2X,F14.12)', s
    ↪ +1, writeflux, writeerr, regsizesr



    END
    ELSE: BEGIN
    print, 'Background for region ', s+1, ' is a polygon
        ↪ with corners:'
    print, bgparams
    poly1regx = bgparams[*, 0] − 1.0
poly1regy = bgparams[*, 1] − 1.0
; now the pixels inside the polygon need to be found: inside
    ↪ .pro
; does this but is also slow for large images, so the
    ↪ computation
; is done in a smaller window which can be significantly
    ↪ faster
; define the window as slightly larger than the polygon
polyminx = MIN(poly1regx, MAX=polymaxx)
polyminy = MIN(poly1regy, MAX=polymaxy)
winborder = 4
windowdata = fitsdata[FLOOR(polyminx−winborder):CEIL(
    ↪ polymaxx+winborder), FLOOR(polyminy−winborder):CEIL(
    ↪ polymaxy+winborder)]
; adjust polygon corners to the extracted window
polywindowx = poly1regx − FLOOR(polyminx−winborder)
polywindowy = poly1regy − FLOOR(polyminy−winborder)
; get the size of the window
windowsize = size(windowdata)
windowsizex = windowsize[1]
windowsizey = windowsize[2]
; create a "mask" array where the information of which
    ↪ pixels are
; inside the background polygon is stored
windowmask = intarr(windowsizex, windowsizey)
; check each pixel in the wondow array to see if they are
    ↪ inside the polygon
FOR i = 0, windowsizex−1 DO BEGIN
    FOR j = 0, windowsizey−1 DO BEGIN
        windowmask[i,j] = inside(i, j, polywindowx,
            ↪ polywindowy)
    ENDFOR
ENDFOR
; find the indices of the polygon pixels
```

```
polypixels = where(windowmask EQ 1, polygcnt)
; calculate values for the polygon pixels
windowtotal = TOTAL(windowdata[polypixels])
polygmean = MEAN(windowdata[polypixels])
polygvar = VARIANCE(windowdata[polypixels])
; subtract the background from the source pixels
bkgsubpolygflux = totalflux − pxcnt * polygmean
bkgsubpolygfluxmean = bkgsubpolygflux / pxcnt
print, 'Polygon mean flux: ', polygmean, ', pixels: ',
    ↪ polygcnt
; compute the total error using the polygon
totalerrpolyg = aperisherr(meanflux, pxcnt, polygvar,
    ↪ polygcnt)
; compute the source region size in sr (image in MJy/sr)
; 1 sq. arcsec = 2.3504*10^−11 sr
pxareasr = 2.3504e−11 * pxscale^2
regsizesr = pxareasr * pxcnt
print, 'Bkg−subtracted total flux [Jy]: ',
    ↪ bkgsubpolygfluxmean * regsizesr * 1e6, ', error: ',
    ↪ totalerrpolyg * regsizesr  * 1e6 / pxcnt

    ;10−sigma correction
; print, 'Excluded pixels with values: ', fitsdata[
    ↪ regpixelssubstracted]
polygtensigma = polygmean + 10 * sqrt(polygvar)
polygmintensigma = polygmean − (10 * sqrt(polygvar))
print, polygtensigma
polypixelsa = where(windowmask EQ 1 AND windowdata lt
    ↪ polygtensigma AND windowdata gt polygmintensigma,
    ↪ polygcnt)
polypixelsb = where(windowmask EQ 1 AND (windowdata gt
    ↪ polygtensigma OR windowdata lt polygmintensigma),
    ↪ polygcntb)
windowtotal = TOTAL(windowdata[polypixelsa])
polygmean = MEAN(windowdata[polypixelsa])
polygvar = VARIANCE(windowdata[polypixelsa])
print, 'Excluded ', polygcntb, ' pixels in the background
    ↪ polygon.'
print, ' with values', windowdata[polypixelsb]

bkgsubpolygflux = totalflux − pxcnt * polygmean
bkgsubpolygfluxmean = bkgsubpolygflux / pxcnt
print, 'Polygon mean flux: ', polygmean, ', pixels: ',
    ↪ polygcnt
; compute the total error using the polygon
totalerrpolyg = aperisherr(meanflux, pxcnt, polygvar,
    ↪ polygcnt)
errpolygmean = totalerrpolyg / pxcnt
```

```
      ; compute the source region size in sr (image in MJy/sr)
      ; 1 sq. arcsec = 2.3504*10^-11 sr
      pxareasr = 2.3504e-11 * pxscale^2
      regsizesr = pxareasr * pxcnt
      print, 'Bkg-subtracted total flux [mJy]: ',
        ↪ bkgsubpolygfluxmean * regsizesr * 1e9, ', error: ',
        ↪ errpolygmean * regsizesr  * 1e9
      writeflux = bkgsubpolygfluxmean * regsizesr * 1e9
      writeerr = errpolygmean * regsizesr  * 1e9
          printf, unit1, FORMAT='(I2,14X,F14.8,2X,F14.9,2X,F14.12)
            ↪ ', s+1, writeflux, writeerr, regsizesr
          ; print, FORMAT='(I2,14X,F14.10,2X,F14.10,2X,F14.10)', s
            ↪ +1, writeflux, writeerr, regsizesr



        END
        ;ELSE: print, 'Background for region ', s+1, ' was
            ↪ misinterpreted.', regidentbg
        ENDCASE
ENDFOR ; s


close, unit1
t2=systime(0,/sec)

print, 'Computation took ', t2-t1, ' seconds'

;————————————————————————————————————————————————————
    ↪


END
```

B Source code of *ds9sourcepars.pro*

```
;+
; NAME:
;     DS9SOURCEPARS
;
; PURPOSE:
;     This function will extract the parameters of a defined
    ↪ source or
;     background region (circle or ellipse as source, circular
    ↪ annullus,
;     elliptical annullus or polygon as background) from a
    ↪ standard ds9
```

```
;          region file and return them as an array
;  INPUT:
;     Calling sequence is result = ds9sourcepars(linestring).
;
;     In: linestring − the full ds9 region file line
;
;  OUTPUT:
;     Output is the parameters:
;          x, y, radius
;          x, y, axis ratio, angle, major axis
;          x, y, inner radius, outer radius
;          x, y, axis ratio, angle, inner major axis, outer major
;    ↪ axis
;          points of the polygon (given units given in the file) in
;    ↪  an array of
;          size (points, 2) that can then be separated into x and y
;    ↪  coordinate
;          vectors.
;−
FUNCTION ds9sourcepars, linestring

   ; read full line and get only point coordinates
   openparent = STRPOS(linestring, '(')
   linelength = STRLEN(linestring)
   relevantlength = linelength − (openparent+1)
   tempstring = STRMID(linestring, openparent+1, relevantlength
      ↪ −1)
   ; dpoints for polygons is the count of all xy pairs, div by
      ↪ two to get
   ; different points
   ; dpoints in general is the amount of parameters which
      ↪ identifies
   ; region type correctly (3=circle, 4=annullus, 5=ellipse, 7=
      ↪ elliptical
   ; annullus. Polygons are even numbers >=6)
   infopieces = STRSPLIT(tempstring, ',', LENGTH=piecelen, count=
      ↪ dpoints)
   parampieces = STRSPLIT(tempstring, ',', /EXTRACT)
   ; infopieces gets the xy pairs for polygons, parampieces the
   ; parameters for other region types
   ; sourceparlist gets info from infopieces/parampieces or
      ↪ combinations,
   ; since elliptical annulli only need 6 parameters to be
      ↪ unambiguous
   ; the order of ellipse parameters is adjusted to fit
      ↪ dist_ellipse
   ;      input format
   CASE dpoints OF
```

```
3:        BEGIN
                sourceparlist = fltarr(3)
                sourceparlist[0] = float(parampieces[0])
                sourceparlist[1] = float(parampieces[1])
                sourceparlist[2] = float(parampieces[2])
                regident = 1
                END
4:        BEGIN
                sourceparlist = fltarr(4)
                sourceparlist[0] = float(parampieces[0])
                sourceparlist[1] = float(parampieces[1])
                sourceparlist[2] = float(parampieces[2])
                sourceparlist[3] = float(parampieces[3])
                regident = 3
                END
5:        BEGIN
                sourceparlist = fltarr(5)
                ellminortemp = float(parampieces[3])
                sourceparlist[0] = float(parampieces[0])
                sourceparlist[1] = float(parampieces[1])
                sourceparlist[4] = float(parampieces[2])
                sourceparlist[2] = sourceparlist[4]/
                    ↪ ellminortemp
                sourceparlist[3] = float(parampieces[4])
                regident = 2
                END
7:        BEGIN
                sourceparlist = fltarr(6)
                ellanninnerminor = float(parampieces[3])
                ellannouterminor = float(parampieces[5])
                sourceparlist[0] = float(parampieces[0])
                sourceparlist[1] = float(parampieces[1])
                sourceparlist[4] = float(parampieces[2])
                sourceparlist[2] = sourceparlist[4]/
                    ↪ ellanninnerminor
                sourceparlist[3] = float(parampieces[6])
                sourceparlist[5] = float(parampieces[4])
                regident = 4
                END
ELSE:     BEGIN
                pointpairs = dpoints/2
                sourceparlist = fltarr(pointpairs,2)
                FOR k = 0, pointpairs−1 DO BEGIN
                        sourceparlist[k, 0] = FLOAT(
                            ↪ STRMID(tempstring,
                            ↪ infopieces[2*k], piecelen
                            ↪ [2*k]))
                        sourceparlist[k, 1] = FLOAT(
```

```
                                          ↪ STRMID( tempstring ,
                                          ↪ infopieces [2∗k+1],
                                          ↪ piecelen [2∗k+1]))
                              ENDFOR
                              regident = 5
                              END
            ENDCASE
            ;print , ' region identifier (1 = circle , 2 = ellipse , 3
                ↪ = circular annullus , 4 = elliptical annullus , 5 =
                ↪ polygon) ', regident
            RETURN, sourceparlist
END
```

C Source code of *aperisherr.pro*

```
;+
; NAME:
;     APERISHERR
;
; PURPOSE:
;     This returns a flux err computed in the aper.pro style .
;
; INPUT:
;     Calling sequence is result = aperisherr(apemean, apepxcnt ,
    ↪ bkgvar , bkgpxcnt)
;
;     In: apemean − mean pixel value in the ON aperture
;          apepxcnt − number of ON aperture pixels
;          bkgvar − the variance in the bkg OFF annulus/area
;          bkgpxcnt − number of pixels in the bkg OFF annulus/area
;
; OUTPUT:
;     Error value .
;−
FUNCTION aperisherr , apemean, apepxcnt , bkgvar , bkgpxcnt

  error1 = apepxcnt∗bkgvar                                ;
     ↪ Scatter in sky values
  error2 = apemean∗apepxcnt      ; Random photon noise
  error3 = bkgvar∗apepxcnt/bkgpxcnt∗apepxcnt  ; Uncertainty in
     ↪ mean sky brightness

  IF ((apemean) LT 0) THEN BEGIN
    error2 = 0.0
    ;print , 'Bkg brighter than source '
  ENDIF
```

```
    totalerr = sqrt(error1 + error2 + error3)

; print , error1 , error2 , error3
; print , 'Region flux and error , native units: ', datassum ,
    ↪ totalerr
; print , 'Region flux and error , Jy: ', datassum*1.8326e−06,
    ↪ totalerr*1.8326e−06


return , totalerr

END
```